CZECH TECHNICAL UNIVERSITY
IN PRAGUE

Faculty of Nuclear Sciences and Physical
Engineering
Department of Physics

Master's thesis

Upsilon meson production in heavy-ion collisions at the STAR experiment

Bc. Oliver Matonoha

Supervisor: Ing. Olga Rusňáková, PhD.

Prague, 2018

ČESKÉ VYSOKÉ UČENÍ TECHNICKÉ
V PRAZE
Fakulta jaderná a fyzikálně inženýrská
Katedra fyziky

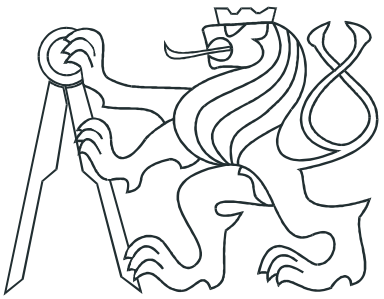

Diplomová práce

Produkce mesonu Upsilon ve srážkách těžkých iontů na experimentu STAR

Bc. Oliver Matonoha

Školitel: Ing. Olga Rusňáková, PhD.

Praha, 2018

Prohlášení:

Prohlašuji, že jsem svou diplomovou práci vypracoval samostatně a použil jsem pouze podklady (literaturu, projekty, software, atd.) uvedené v přiloženém seznamu.

Nemám závažný důvod proti užití tohoto školního díla ve smyslu § 60 Zákona č. 121/2000 Sb., o právu autorském, o právech souvisejících s právem autorským a o změně některých zákonů (autorský zákon).

V Praze dne

Bc. Oliver Matonoha

Title:

Upsilon meson production in heavy-ion collisions at the STAR experiment

Author: Bc. Oliver Matonoha

Specialisation: Experimental nuclear and particle physics

Sort of project: Master's thesis

Supervisor: Ing. Olga Rusňáková, PhD.

Abstract:
In ultra-relativistic heavy-ion collisions, creation of a novel state of matter is expected, in accordance with predictions by lattice QCD calculations. Under such extreme conditions, regular hadronic matter undergoes a phase transitions and forms a plasma of deconfined quarks and gluons (QGP). This medium is hypothesised to comprise the universe in its earliest stages. Researching the QGP properties can bring valuable input for early cosmological models as well as help us understand the character of the strong interaction.

Production of the quarkonium mesons is a crucial probe of the QGP, since their suppression can be viewed as a direct evidence of the plasma formation, due to the colour screening effect. Moreover, this can be used to infer constraints on the QGP temperature.

In this thesis, author's analysis of the Υ production at the STAR experiment in Au+Au collisions at $\sqrt{s_{\mathrm{NN}}} = 200$ GeV via the di-electron decay channel is presented. The nuclear modification factors for the ground state and for the excited states are reported. At RHIC energies, secondary effects complicating the measured suppression are deemed less significant for the Υ, which makes it a cleaner probe of the screening effect.

Key words: heavy-ion collisions, quark-gluon plasma, upsilon, quarkonium suppression, STAR

Název diplomové práce:

Produkce mesonu Upsilon ve srážkách těžkých iontů na experimentu STAR

Autor: Bc. Oliver Matonoha

Obor: Experimentální jaderná a částicová fyzika

Školitel: Ing. Olga Rusňáková, PhD.

Abstrakt:

Dle předpovědí QCD na mřížce se očekává, že v ultra-relativistických srážkách těžkých iontů dochází k vytvoření nového stavu hmoty. Za přítomných extrémních podmínek podstupuje běžná hadronová hmota fázový přechod a formuje plasma dekonfinovaných kvarků a gluonů (QGP). Je předpokládáno, že toto médium tvořilo vesmír v jeho nejranějších momentech. Zkoumání vlastností QGP může přinést cenné podněty pro kosmologické modely a vést k lepšímu pochopení charakteru silné interakce.

Produkce kvarkonií patří mezi zásadní sondy ke zkoumání QGP. Jejich potlačení lze chápat jako přímý důsledek vytvoření plasmatu kvůli barevnému stínění. Z měřené produkce lze rovněž vyvozovat limitní hodnoty teplot QGP.

V této práci autor představuje svou analýzu produkce mesonu Υ na experimentu STAR ve srážkách Au+Au při $\sqrt{s_{\mathrm{NN}}} = 200$ GeV za pomocí dvoj-elektronového rozpadového kanálu. Finálním výsledkem jsou jaderné modifikační faktory, které jsou ukázány pro základní i excitované stavy. Sekundární vlivy komplikující interpretaci naměřeného potlačení produkce jsou pro Υ při energiích na RHICu považovány za méně významné. To činí z Υ čistší sondy ke studování barevného stínění.

Klíčová slova: srážky těžkých iontů, kvark-gluonové plasma, upsilon, potlačení kvarkonií, STAR

Acknowledgement

I would like to express my sincere gratitude to Dr. Rusňáková, Dr. Bielčík, and Prof. Reed for their invaluable guidance on my research, and to my parents for their endless support during my studies.

Contents

Introduction **1**

1 Collisions of ultra-relativistic heavy nuclei **3**
1.1 Motivation for heavy-ion collisions physics 3
1.2 Event kinematics and geometry 4
1.3 Collision geometry and event activity 4
1.4 Nuclear modification factor 6

2 Quark-gluon plasma **9**
2.1 QCD matter and the phase diagram 9
2.1.1 Bag model of a hadron 10
2.1.2 Deconfinement temperature in the bag model 12
2.2 Characteristics of the medium 13
2.2.1 Space-time evolution in heavy-ion collisions 13
2.2.2 Collective anisotropic flow 13
2.2.3 Secondary particle production by coalescence 15
2.3 Tomography of the QGP with hard probes 17

3 Heavy quarkonia **19**
3.1 Fundamental properties 19
3.1.1 Decay channels and feed-down 20
3.1.2 Prompt quarkonium production 23
3.2 Dissociation by the Debye colour screening 23
3.2.1 Quarkonium potential and J/ψ suppression 24
3.2.2 Sequential melting – QGP thermometer 28
3.3 Statistical recombination 29
3.4 Cold nuclear matter effects 30

3.4.1 Nuclear shadowing . . . 32
3.4.2 Quarkonium suppression by hadrons . . . 35

4 Experimental setup **39**
4.1 The RHIC accelerator facility . . . 39
4.2 The STAR experiment . . . 40
4.2.1 Time Projection Chamber . . . 41
4.2.2 Barrel Electromagnetic Calorimeter . . . 43

5 Author's analysis on $\Upsilon \to e^+e^-$ **47**
5.1 Dataset and tools . . . 47
5.1.1 Event selection . . . 48
5.1.2 Event centrality . . . 48
5.2 Upsilon reconstruction . . . 49
5.2.1 Selection with TPC . . . 51
5.2.2 Selection with BEMC . . . 51
5.3 Raw yield reconstruction . . . 52
5.3.1 Combinatorial background . . . 52
5.3.2 Event mixing . . . 55
5.3.3 Upsilon signal line-shapes . . . 56
5.3.4 Correlated background . . . 57
5.3.5 Signal extraction . . . 58
5.4 Reconstruction efficiency and detector acceptance . . . 61
5.4.1 Embedding . . . 61
5.4.2 Daughters acceptance, trigger efficiency, tracking . . . 61
5.4.3 BEMC-PID efficiency . . . 62
5.4.4 TPC-PID efficiency . . . 62
5.4.5 Total reconstruction efficiency . . . 64
5.5 Nuclear modification factor . . . 64
5.6 Discussion . . . 69

Summary **71**

References **73**

Appendix **I**
A Published papers and posters related to this work . . . I

List of Figures

1.1 Monte Carlo Glauber model event 5
1.2 Multiplicity and centrality 6

2.1 QCD phase diagram 10
2.2 Heavy-ion collision space-time evolution 14
2.3 Anisotropic flow 15
2.4 Elliptic flow coefficient v_2 16
2.5 Hadron production in QGP 16
2.6 Hard probes in QGP 17
2.7 Jet quenching 18

3.1 Charmonia and bottomonia families 21
3.2 Debye colour charge screening 24
3.3 Quarkonium potential 27
3.4 Anomalous suppression of J/ψ 28
3.5 Sequential melting of quarkonia 29
3.6 J/ψ suppression at the LHC and RHIC 30
3.7 Regeneration due to charm abundance 31
3.8 Elliptic flow of J/ψ at the LHC and RHIC 31
3.9 Gluon density in a nucleon 33
3.10 Shadowing ratio 33
3.11 J/ψ suppression in p+Pb collisions 34
3.12 Nuclear absorption of J/ψ 36
3.13 Suppression of $\psi(2S)$ in p+Pb collisions 37

4.1 The RHIC accelerator complex 40
4.2 The STAR experiment 42
4.3 The TPC detector 42

4.4 TPC PID via specific energy loss 44
4.5 The BEMC detector 44
4.6 BEMC PID via energy-momentum ratio 45

5.1 Primary vertex position distributions 49
5.2 Centrality related distributions 50
5.3 Upsilon reconstruction method 50
5.4 TPC PID distributions 52
5.5 Distribution of the kinematics variables 53
5.6 Pair kinematics distributions 54
5.7 BEMC related distributions 54
5.8 Combinatorial background 56
5.9 Invariant mass spectrum 59
5.10 Invariant mass spectrum – centrality dependence 60
5.11 TPC acceptance and trigger efficiency 62
5.12 Tracking efficiency 63
5.13 BEMC-PID efficiencies 63
5.14 Fits of $n\sigma_e$ distribution 65
5.15 TPC-PID efficiency 66
5.16 Total efficiency – contributions 66
5.17 Total efficiency – centrality dependence 67
5.18 Nuclear modification factor of $\Upsilon(1S)$ and $\Upsilon(2S+3S)$ 68
5.19 Nuclear modification factor – combined results 70

Introduction

Equipped with his five senses, man explores the universe around him and calls the adventure Science.

—Edwin Powell Hubble

Search for unknown has always been one of the most driving motives of humanity. Be it a colonisation of far lands, or the race for space, people have always found it intriguing to step into territories previously unknown to humankind. Similarily, particle physicists strive to push the frontiers of knowledge about the very substance of which reality is built and interestingly, by examining some of the tiniest particles, they can learn something new about even the universe itself.

One of the most alluring subjects of today high energy physics is the quark-gluon plasma (QGP). It is an absolutely singular state of matter believed to fill the universe few microseconds after the Big Bang. Such extreme medium can come into existence naturally only under the most extraordinary conditions themselves and one method to access them is by colliding heavy nuclei at ultra-relativistic energies.

The objective of this Master's thesis is to describe the physics of QGP and heavy quarkonia, which can be used to study the plasma temperature, as well as to introduce the author's original analysis on production of the Υ quarkonium at the STAR experiment.

Chapter 1

Collisions of ultra-relativistic heavy nuclei

This chapter serves as an introduction to the thesis' work. Kinematics and variables used to describe a collision event and its key concepts are introduced.

1.1 Motivation for heavy-ion collisions physics

Physics of heavy-ion collisions is a field of high energy physics studying collisions of massive atomic nuclei at ultra-relativistic energies. One of its principal motivations for this is the possible creation of the quark-gluon plasma (QGP) and its further analysis. Researching the QGP properties helps us understand the state of the universe in its earliest moments as well as the character of the strong interaction, which is described by the theory of quantum chromodynamics (QCD).

Heavy-ion collisions are studied at large particle accelerators—most notably RHIC and the LHC. Such collisions are *extreme* from various points of view. For instance, the hottest medium observed on Earth is created. The QGP is also found out to be the most vortical fluid, spinning up to 10^{22} per second. Its magnetic field is expected to be the strength of 10^{14} T, which is more than a thousandfold of the strongest magnetic field sources in the

universe—the magnetars.

1.2 Event kinematics and geometry

For the sake of conciseness, one uses *natural units* ($c, \hbar = 1$) in high energy physics problems. A heavy-ion collision is characterised by its centre-of-mass collision energy per nucleon pair $\sqrt{s_{\mathrm{NN}}}$. Particles coming from such collisions are then described with their Lorentz-invariant four-vectors $\mathbf{x} = (t, x, y, z)$, $\mathbf{p} = (E, p_x, p_y, p_z) = (E, p_{\mathrm{T}}, p_z)$. A following set of coordinates is also used for a laboratory frame centered around $x = y = z = 0$ (interaction point): φ (azimuthal angle), η (pseudorapidity), r (radius). The η is a function of polar angle θ—$\eta = -\log(\tan\frac{\theta}{2})$—and, for high-momentum particles $p \geq m$, is an approximation of rapidity relative to the beam $y = \frac{1}{2}\frac{E+p_z}{E-p_z}$. Rapidity is convenient mostly because it transforms additively under Lorentz boosts, unlike velocity. In these coordinates, following relations are valid:

$$p_x = |\vec{p_T}| \cos\varphi \ , \tag{1.1}$$

$$p_y = |\vec{p_T}| \sin\varphi \ , \tag{1.2}$$

$$p_z = |\vec{p}| \sinh\eta \ . \tag{1.3}$$

Oftentimes it is also convenient to work with the *transverse mass*. It is Lorentz-invariant and for an object with rest mass m, it is defined as follows,

$$m_{\mathrm{T}}^2 = p_{\mathrm{T}}^2 + m^2 \ . \tag{1.4}$$

1.3 Collision geometry and event activity

Heavy-ion collisions are in essence collisions of two clusters of fluctuating nucleons and as such have many collision geometry configurations, which is an important factor for many

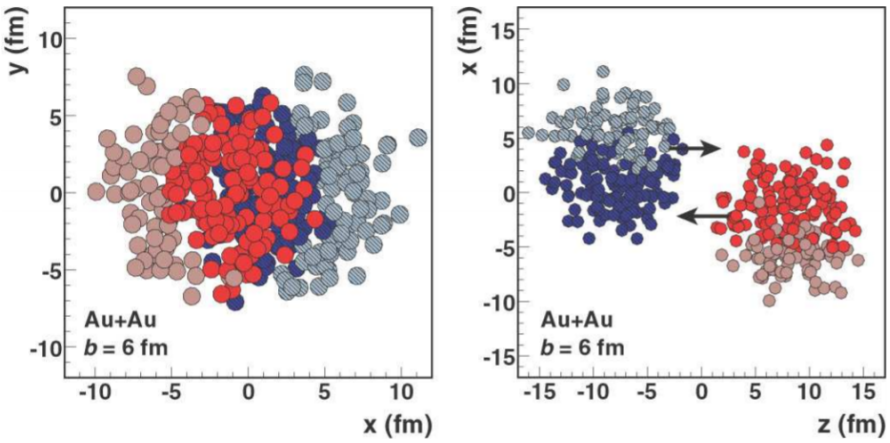

Fig. 1.1: Illustration of a Au+Au $\sqrt{s_{\mathrm{NN}}} = 200$ GeV event in the Monte Carlo Glauber model. Highlighted nucleons represent the participants, unemphasised ones the spectators. Taken from [2].

processes. Impact parameter b is one of the variables used to describe said geometry. It is defined as the relative distance between the two nuclei centres in a plane transverse to the beam axis. Collisions with smaller b have generally larger energy densities and temperatures.

Another important variable is the number of participants N_{part} and the number of binary nucleon collisions N_{coll}. The participants are those nucleons which actively participate in the collision, ie. have at least one interaction. Nucleons that are not participant are called the spectators. The N_{part} and N_{coll} are particularly important for normalisation purposes—soft probes (low energy transfer) are expected to scale proportionally with the N_{part}, whereas hard probes (high energy transfer) with the N_{coll} [1]. Relating the impact parameter and the mean number of participants and binary collisions is usually done with Monte Carlo Glauber model [2]. Example of an event in the MC Glauber model is shown in Fig. 1.1.

As implied, the mentioned variables are not physically measurable. One thus also works with centrality, a percentage of the total nuclear interaction cross section. It is usually inferred from the total transverse energy E_{T} or the charged particle density N_{ch} (also called multiplicity). The approximate relations between the centrality, b, N_{part}, N_{ch}, and the collision geometry are illustrated in Fig. 1.2.

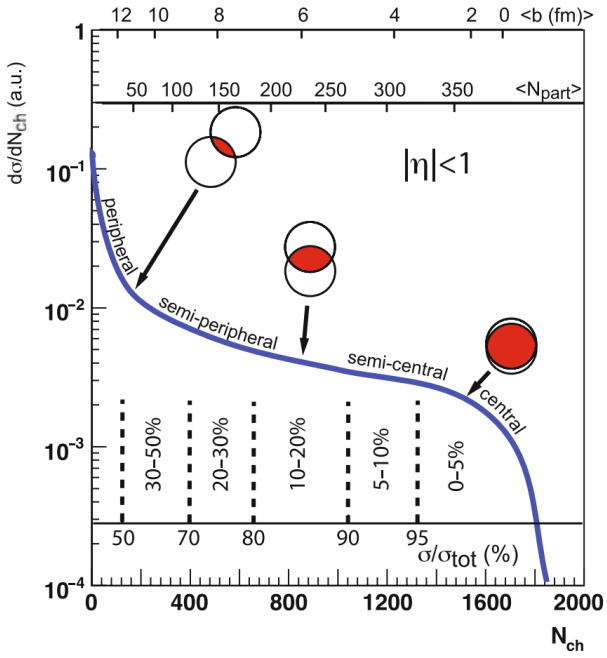

Fig. 1.2: Cartoon of a distribution in final-state charged particle multiplicity. Connections with centrality, b, and $\langle N_{\rm part} \rangle$ can be seen. Taken from [3].

1.4 Nuclear modification factor

Difference in the production between proton-proton collisions and heavy-ion collisions is quantified via the nuclear modification factor $R_{\rm AA}$. It is equal to unity if no net medium effects are observed and zero if complete suppression is measured. For hard probes, in its simplest form, it is defined as follows,

$$R_{\rm AA} = \frac{Y_{\rm AA}}{N_{\rm coll} \times Y_{\rm pp}} \ , \tag{1.5}$$

where $Y_{\rm AA}$ and $Y_{\rm pp}$ are adequately normalised quarkonium yields in A+A and p+p collisions, respectively.

Chapter 2

Quark-gluon plasma

This chapter serves as an overview of the quark-gluon plasma (QGP), a novel state of matter created in ultra-relativistic collisions of heavy nuclei. First, we determine the phase transition temperature from a phenomenological bag model approach. Then, we describe the properties of the medium and potential means to study it.

2.1 QCD matter and the phase diagram

Lattice QCD calculations predict that under extreme conditions, hadronic matter undergoes a phase transition and becomes a plasma of deconfined quarks and gluons. Observations of a strongly interacting near-perfect liquid (sQGP) have been made in the early 2000's in heavy-ion collisions at the RHIC collider in Brookhaven National Laboratory. Its signatures are consistent with those of the QGP.

Studies of the QGP are of great importance. For instance, QGP is believed to comprise the universe a few microseconds after the Big Bang [19]. Therefore, measurements of the QGP properties and determination of e.g. its equation of state have large implications for early-cosmological models. Moreover, QGP studies also bring valuable insights on phenomena in the non-perturbative regimes of QCD, such as the hadronisation. That being said, the QGP is still a large unknown. Of what type is the phase transition from hadronic matter to

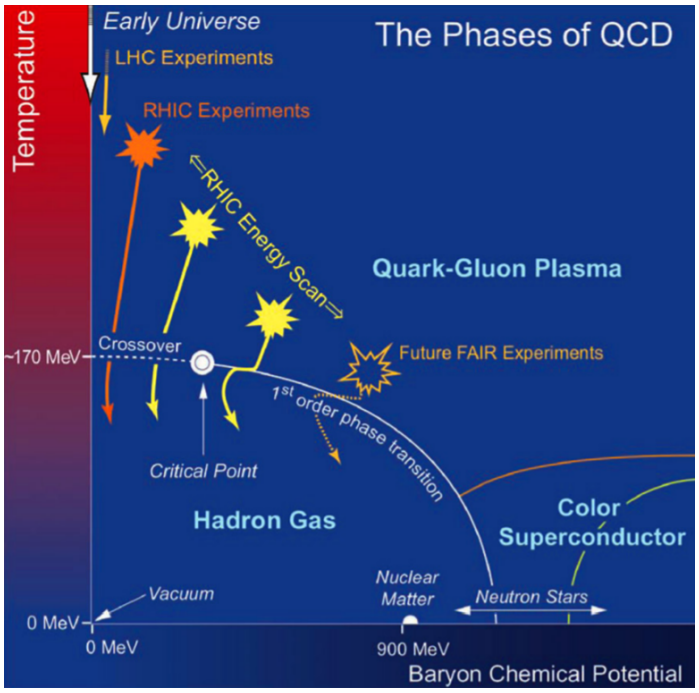

Fig. 2.1: Phase diagram of QCD matter with boundaries defining various states and the phase transitions between them. Some expected occurences of the given T or μ_b are also shown. Taken from [4].

QGP? How does the fireball of deconfined quarks and gluons transforms into a hadron gas? Is there a restoration of chiral symmetry? These are only some of the plethora of unanswered questions.

QCD matter undergoes the phase transition if the temperature T and/or baryon chemical potential μ_b are sufficiently high. Regimes of high T are accessed at leading world's heavy-ion accelerators, i.e. the LHC or RHIC. Conditions with large μ_b (net baryon density) are expected to be present for instance in neutron stars. The QCD phase diagram is shown in Fig. 2.1.

2.1.1 Bag model of a hadron

Hadrons can be viewed as quarks confined in 'bubbles' or 'bags' of empty vacuum, surrounded by a non-perturbative QCD vacuum exerting pressure, which can be naively thought of as

a liquid of gluon-gluon pairs [5]. Let us know consider massless free fermions in a spherical cavity of radius R. They are governed by the Dirac equation, which reads

$$\gamma \cdot p\psi = 0 \ , \tag{2.1}$$

where γ are the γ-matrices in the Dirac representation and ψ the fermion four-component wave function. The lowest energy solution of this equation is the $(S_{1/2})$ state and its form is as follows,

$$\psi_+(r,t) = N \exp(-ip^0 t)\, j_0(p^0 r)\chi_+ \ , \tag{2.2}$$

$$\psi_-(r,t) = N \exp(-ip^0 t)\, \vec{\sigma} \cdot \hat{r}\, j_1(p^0 r)\chi_- \ , \tag{2.3}$$

where $\psi = \left(\begin{smallmatrix}\psi_+\\ \psi_-\end{smallmatrix}\right)$, N is a normalisation constant, j_i the i-th order Bessel function, and χ the spinors. The assumption of confinement within the cavity corresponds to the condition that at $r = R$, the scalar density $\psi\bar{\psi}$ goes to zero[1]. This leads to

$$[j_0(p^0 R)]^2 - \vec{\sigma} \cdot \hat{r}\, \vec{\sigma} \cdot \hat{r}\, [j_1(p^0 R)]^2 = 0 \tag{2.4}$$

$$[j_0(p^0 R)]^2 - [j_1(p^0 R)]^2 = 0$$

$$\rightarrow p^0 R = 2.04 \ . \tag{2.5}$$

The kinetic energy of the quarks in the bag is thus inversely proportionate to the radius R. Effect of the confinement can be represented phenomenologically by the bag pressure B, which is equal to the difference between the energies of the empty and the QCD vacuum. Energy of a bag of N quarks is therefore

$$\begin{aligned} E(R) = & N \cdot \frac{2.04}{R} && \rightarrow \text{tries to expand the bag} \\ & + \frac{4\pi}{3} B R^3 && \rightarrow \text{tries to contract the bag} \ . \end{aligned} \tag{2.6}$$

[1]Equivalently, the condition that the normal component of the vector current $\bar{\psi}\gamma_\mu\psi$ vanishes at $r = R$ can be used.

From this we can see that the hadron radius stems from an interplay of the outwards going kinetic pressure and the inwards going bag pressure, and equilibrates at $\frac{dE}{dR} = 0$, which leads to the relation

$$B^{1/4} = (\frac{2.04N}{4\pi})^{1/4} \frac{1}{R} \ . \tag{2.7}$$

Now, using a proton for instance ($R \simeq 0.8$ fm, $N = 3$), the value of the bag pressure can be estimated as $B^{1/4} = 206$ MeV.

2.1.2 Deconfinement temperature in the bag model

Let us now consider a gas of free quarks and gluons within the cavity of volume V. Total pressure of such gas of relativistic massless particles can be calculated as follows,

$$P = (g_g + \frac{7}{8} g_q) \frac{\pi^2}{90} T^4 \ , \tag{2.8}$$

where g are the degeneracy numbers. For gluons, this is $g_g = 8 \times 2 = 16$ (colour, polarisation), and for quarks $g_q = 2 \times 2 \times 3 \times 2 = 24$ (quarks vs antiquarks, flavour, colour, polarisation).

We would expect the deconfinement to set in when the kinetic pressure of this gas exceeds the QCD-vacuum bag pressure B. This happens at the critical temperature

$$T_c = (\frac{90}{37\pi^2})^{1/4} B^{1/4} \ , \tag{2.9}$$

and for the previously estimated value of $B^{1/4} = 206$ MeV, this gives $T_c \simeq 144$ MeV. Despite the fact that the bag model is very simple, this is very close to today's estimates from lattice QCD of $T_c = 156$ MeV [2]. [6][7]

[2] To put these numbers into perspective, the $T_c = 156$ MeV corresponds to $\approx 2 \times 10^{12}$ K, which is 100000× hotter than the Sun's core!

2.2 Characteristics of the medium

2.2.1 Space-time evolution in heavy-ion collisions

A diagram of the space-time evolution in heavy-ion collisions with the creation of the QGP is shown in Fig. 2.2. A scenario without the creation of the deconfining medium is also included. In the current paradigm, the phases could be described as follows,

1. Pre-equilibrium stage ($\tau \equiv \sqrt{t^2 - z^2} \lesssim 1$ fm/c); scatterings with the highest momentum transfer Q^2 take place, producing the hardest particles,

2. Thermalisation ($1 \lesssim \tau \lesssim 10$ fm/c); quarks and gluons are abundantly created and the system reaches sufficient temperature and energy density for the fireball of deconfining medium to be formed, in which partons can subsequently reach a local thermal equilibrium,

3. Hadronisation ($\tau \sim 20$ fm/c)[3]; after the fire-ball has expanded and cooled down, hadronisation occurs at the chemical freeze-out, which fixes the chemical content of the system,

4. Thermal freeze-out; hadrons no longer interact inelastically and their kinematical spectra become fixed.

2.2.2 Collective anisotropic flow

Collective anisotropic flow of light quarks has been the key evidence for the creation of a strongly coupled, near perfectly liquid, plasma. In non-central collisions of heavy ions, the fireball has an 'almond' shape in the xy-plane, which can be characterised by its eccentricity

$$\varepsilon_2 = \frac{\sigma_y^2 - \sigma_x^2}{\sigma_y^2 + \sigma_x^2} \,, \tag{2.10}$$

[3]This is still very far from when the particles hit detectors, which is on the order of cm/c to m/c.

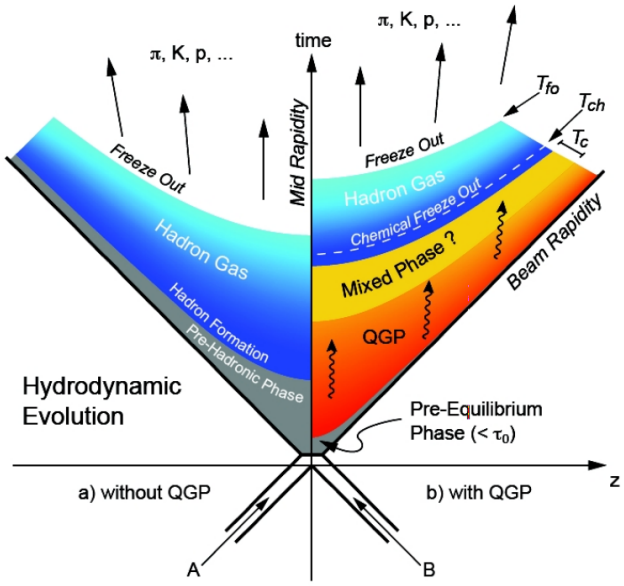

Fig. 2.2: Diagram of the space-time evolution of a heavy-ion collision in the scenario with QGP creation (*right*) or without (*left*). Taken from [8].

where $\sigma^2_{x,y}$ are variances of the x- or y-projections of the distribution of participant nucleons. Assuming that the system reaches a thermal equilibrium, this initial-state geometrical anisotropy translates into anisotropic expansion of the fireball and consequently, into final-state anisotropy in azimuthal distribution of emitted particles. This is because there are different pressure gradients in the medium, due to the uneven distribution of matter. Pressure gradients in direction parallel to the impact parameter $\vec{b}$ are greater than in the one perpendicular, which results in a preferred direction of emission.

Experimentally, the collective flow anisotropies can be quantified with Fourier coefficients v_n of the azimuthal distribution of particles, i.e.

$$E\frac{d^3N}{d^3p} = \frac{1}{2\pi}\frac{d^2N}{p_{\mathrm{T}}\,dp_{\mathrm{T}}\,dy} \times \left(1 + \Sigma_{n=1}^{\infty} 2v_n \cos(n(\varphi - \psi^{EP}))\right) , \tag{2.11}$$

where N is the number of particles with energy E, transverse momentum p_{T}, rapidity y, and azimuthal angle φ, and ψ^{EP} is the angle of the event plane, which is an experimental approximation of the a priori unknown reaction plane defined by the $\vec{b}$ and z. The second-

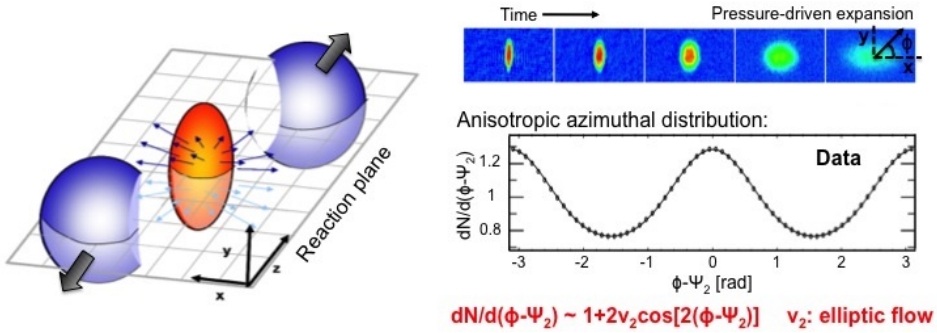

Fig. 2.3: Picture representing the anisotropies of initial-state geometry (*left*), fireball expansion (*top right*), and azimuthal distribution of particles (*bottom right*). Taken from [9].

order coefficient v_2 corresponding to *elliptic flow* has been studied most, even though higher-order ones are also measured. A picture of the collision geometry, anisotropic expansion, and elliptic flow is shown in Fig. 2.3.

Dependences of the v_2 on p_{T} and collision centrality for charged particles measured at ALICE at $\sqrt{s_{\mathrm{NN}}} = 2.76$ TeV are plotted in Fig. 2.4. We can see that the v_2 is stronger in peripheral collisions than in the most central ones, which reflects the difference in the ε_2 of the initial-state geometries. At the LHC, the v_2 magnitude reaches maximum at ~ 3 GeV/c and then starts slowly falling down, consistent with the expectation that extremely hard particles suffer from the effects of QGP negligibly.

2.2.3 Secondary particle production by coalescence

Experimental observations—such as the fact that baryons acquire approximately $\frac{3}{2}\times$ more elliptic flow than mesons of the same mass [11] or that the baryon-to-meson production ratio is significantly enhanced in central collisions [12]—suggest that the dominant method of hadron production in A+A collisions is not fragmentation. In fact, the dense plasma of deconfined partons is expected to give rise to another means of hadronisation—clustering of neighbouring quarks, also called *coalescence*. Cartoons depicting hadron production by fragmentation and by coalescence can be found in Fig. 2.5.

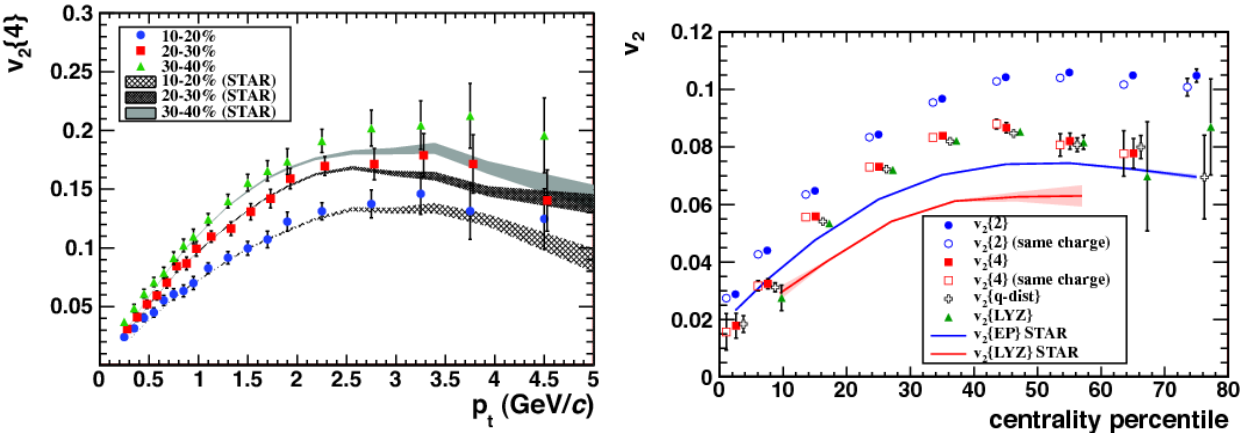

Fig. 2.4: Elliptic flow as a function of p_{T} (*left*) and centrality (*right*). Different sets of datapoints in the right plot represent different approaches in the determination of the v_2. Taken from [10].

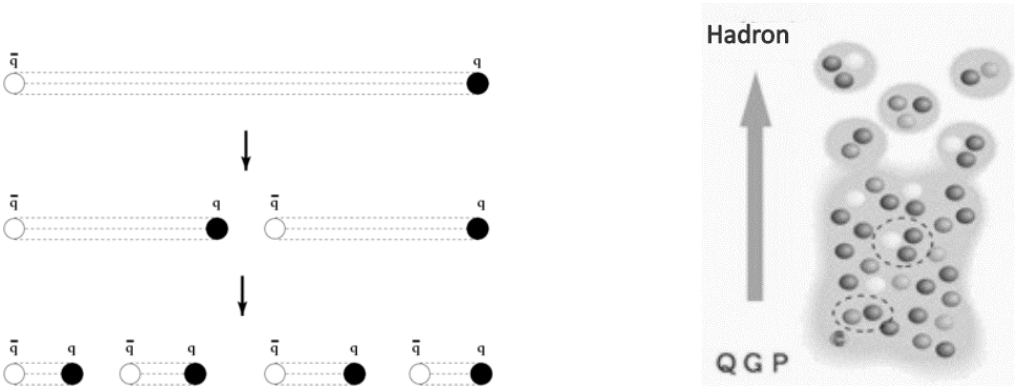

Fig. 2.5: Cartoons of hadron production mechanisms: fragmentation of the binding QCD string (*left*) and coalescence of the deconfined quarks (*right*). Taken from [13][14].

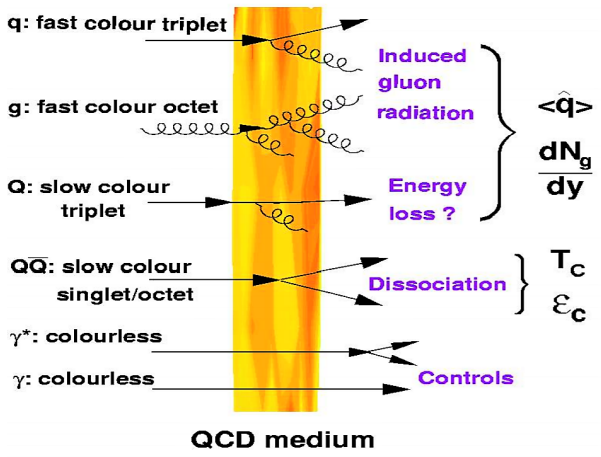

Fig. 2.6: Diagram of the different hard probes, their behaviour in the QGP, and their usage. Q represent heavy quarks, $\langle\hat{q}\rangle$ is a transport coefficient, $\frac{dN_g}{dy}$ initial gluon density; and T_c, ε_c the critical temperature and energy density respectively. Taken from [15].

2.3 Tomography of the QGP with hard probes

Particles with large momentum or masses, referred to as hard probes, are instrumental in tomographic studies of the QGP. They

- are created in the collision's earliest stages from hadronic scatterings with high Q^2, in time-scales of $\sim m_{\mathrm{T}}^{-1} \lesssim 0.1$ fm/c, and thus can experience (and be influenced by) the entire evolution of the medium;
- their cross-sections are quantitatively well described by perturbative QCD (pQCD) calculations.

A diagram of various hard probes, their behaviour in the QGP, and the information they reveal, can be seen in Fig. 2.6.

One of the key mechanisms employing hard probes to study the QGP is *jet quenching*. Jets are characteristic collimated sprays of hadrons coming from fragmentation of a highly virtual parton. Due to conservation of energy, there should (almost) always be at least two jets in an event. That being said, there is a significant dijet asymmetry in central A+A

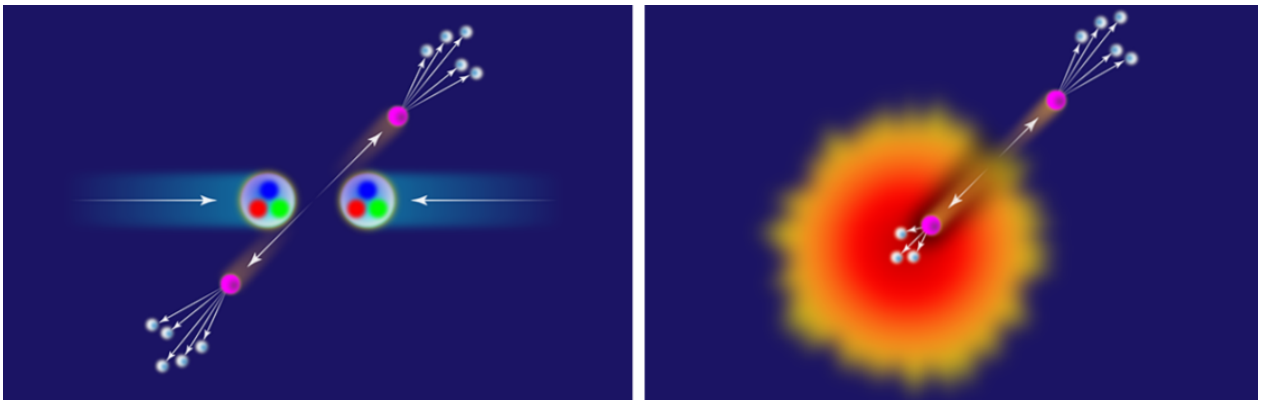

Fig. 2.7: Cartoon illustrating the quenching of jets in quark-gluon plasma and its difference w.r.t. elementary hadron collisions . Taken from [16].

collisions. It can be explained by considering a path-dependent energy loss for the parton traversing the QGP. In instances where jets start from outer regions of the fireball, one of the fragmenting partons can escape relatively unscathed, whereas the recoil parton might get *quenched* in the medium, giving rise to the asymmetry. We show this phenomenon in a cartoon in Fig. 2.7.

Chapter 3

Heavy quarkonia

This chapter focuses on heavy quarkonia, bound systems of heavy quarks and antiquarks of the same flavour. Heavy quarks are important probes to heavy-ion collisions. This is mainly due to the fact, that thanks to their large mass, they are created in early pre-plasma stages. Their mesons are *open heavy flavour* mesons ($c\bar{u}$, $\bar{b}d$, ...) and, much less abundant, the *quarkonia*[1] ($c\bar{c}$, $b\bar{b}$). First, we will introduce the characteristics and behaviour of the latter, namely the ground states J/ψ and $\Upsilon(1S)$, and illustrate how can they be utilised to infer crucial information about the QGP. Relevant cold nuclear matter effects unrelated to the hot QGP phase are also described.

3.1 Fundamental properties

There are many members of the *charmonium* and *bottomonium* families. For the most important s-wave and p-wave vector states, we show the mass, binding energy, and the hadronic radius in Tab. 3.1. Diagrams of the various charmonium and bottomonium states and the possible decay transitions between them can be found in Fig. 3.1.

In heavy-ion experiments, most attention is given to the ground states J/ψ and $\Upsilon(1S)$. This is thanks to the fact that they are relatively easily measurable in di-lepton channels

[1] Also called *hidden charm* or *hidden beauty*, because the overall charm/beauty quantum number is zero.

States	J/ψ	χ_c	ψ'	$\Upsilon(1S)$	χ_b	$\Upsilon(2S)$	χ_b'	$\Upsilon(3S)$
Mass [GeV]	3.07	3.53	3.68	9.46	9.99	10.02	10.26	10.36
Binding energy [GeV]	0.64	0.20	0.05	1.10	0.67	0.54	0.31	0.20
Radius [fm]	0.25	0.36	0.45	0.14	0.22	0.28	0.34	0.39

Tab. 3.1: Mass, binding energy, and radii of common quarkonia states of charm and bottom family. Taken from [3].

and, more importantly, they created mostly before the QGP and, if unaffected, decay long after it disappears—thus have the potential to probe its entire evolution:

$$t^{Q\bar{Q}}_{\text{creation}} < t^{QGP}_{\text{creation}} < t^{QGP}_{\text{lifetime}} \ll t^{Q\bar{Q}}_{\text{lifetime}} \ . \tag{3.1}$$

Furthermore, due to their large binding energy, they exhibit a unique behaviour in the collisions and help in determining the created medium temperature.

3.1.1 Decay channels and feed-down

Most notable decay channels of the important quarkonia are listed in Tab. 3.2, along with the mass widths and the branching ratios. For the J/ψ and the Υ states, the di-electron and di-muon channels are relatively easily accessible. The χ states decay mostly by de-excitation into lower s-wave states via emission of a soft γ, as is illustrated in Fig. 3.1.

This secondary production of lower states from decays of higher excited states is referred to as feed-down. It is absolutely crucial to bear this in mind when interpreting any measured suppression of what is inclusively measured, as the feed-down may account for a very sizable contribution. It is rather difficult to determine this precisely, however an estimate for the $\Upsilon(1S)$ can be found in Tab. 3.3. For the J/ψ, a feed-down contribution of $\sim 33\%$ is expected [17].

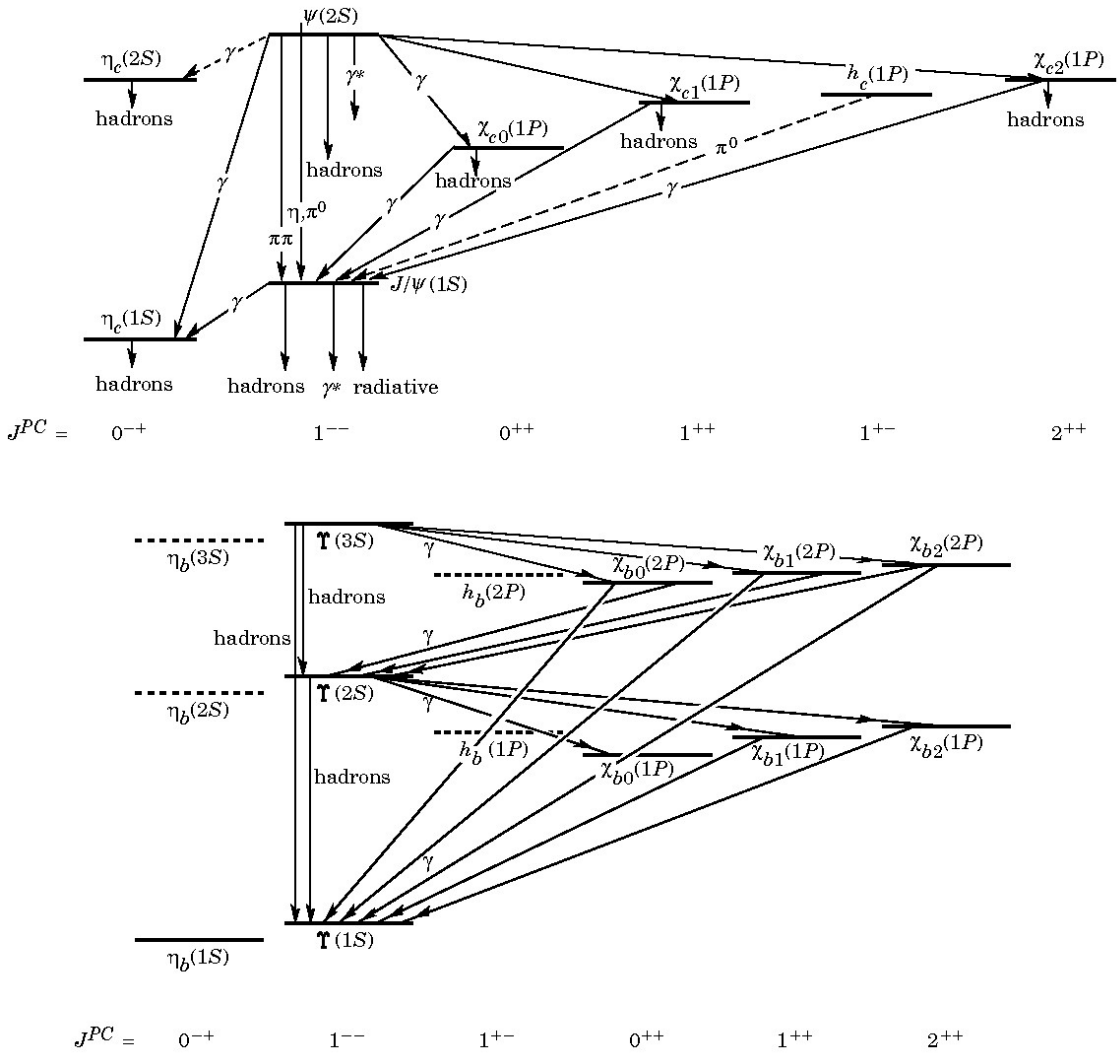

Fig. 3.1: Diagrams of the bound states of the charmonia family (*top*) and the bottomonia family (*bottom*). The ψ' state is denoted as $\psi(2S)$. Vertical position of the bound states represent their mass and additional quantum numbers are shown at the bottom of each diagram. Some decay modes of the states are also displayed. Taken from [20].

Quarkonium	Mass [GeV]	Width [keV]	Decay channel	BR
J/ψ	3.097	92.9	$\rightarrow$hadrons	87.7
			$\rightarrow e^+e^-$	6.0
			$\rightarrow \mu^+\mu^-$	6.0
$\psi(2S)$	3.686	298	$\rightarrow J/\psi + X$	61.0
			$\rightarrow e^+e^-$	$8{\cdot}10^{-3}$
$\Upsilon(1S)$	9.460	54.0	$\rightarrow$hadrons	86.9
			$\rightarrow e^+e^-$	2.4
			$\rightarrow \mu^+\mu^-$	2.5
$\Upsilon(2S)$	10.023	32.0	$\rightarrow \Upsilon(1S) + X$	26.5
			$\rightarrow e^+e^-$	1.9
			$\rightarrow \mu^+\mu^-$	1.9
$\Upsilon(3S)$	10.036	20.3	$\rightarrow \Upsilon(2S) + X$	10.6
			$\rightarrow \Upsilon(1S) + X$	6.6
			$\rightarrow \mu^+\mu^-$	2.2

Tab. 3.2: Interesting decay channels of significant quarkonia. The branching ratio BR is presented for each decay mode. Quarkonia states mass and width are also shown. Values taken from [20].

Prompt $\Upsilon(1S)$	$\sim 51\%$
$\Upsilon(1S)$ from χ_b decays	$\sim 27\%$
$\Upsilon(1S)$ from χ_b' decays	$\sim 10\%$
$\Upsilon(1S)$ from $\Upsilon(2S)$ decays	$\sim 11\%$
$\Upsilon(1S)$ from $\Upsilon(3S)$ decays	$\sim 1\%$

Tab. 3.3: Contributions to the production of $\Upsilon(1S)$. Taken from [18].

3.1.2 Prompt quarkonium production

Although the creation of heavy quarks is relatively well calculable within perturbative QCD, the production of quarkonia is not well-understood. Mechanisms of how do the constituent quarks hadronise, i.e. form a colour-singlet state, still remains a mystery. They are large-distance, low-momentum processes, and thus not easily describable in pQCD. Generally, there have been three approaches to modelling the production: Colour Evaporation Model (CEM), Colour Singlet Model (CSM), and Colour Octet Model employing Non-relativistic QCD (COM+NRQCD). For more information about them, refer to [19][6].

3.2 Dissociation by the Debye colour screening

Historically, the basic deconfining mechanism of hadrons in the QGP has been identified with the Debye screening of the colour charge [21], analogously to the case of electric charge screening in electrolytes or regular plasma. In this description, deconfinement sets in if the hadron binding radius r_H is larger than the Debye screening radius r_D. This radius is inversely proportionate to the temperature of the medium. A cartoon depicting the dissociation by Debye screening is shown in Fig. 3.2.

Usually, the Debye radius is calculated from lattice gauge theory of QCD by calculating the correlation function of a static $Q\bar{Q}$ system in a gluon heat bath. The approximation resulting from these calculations is

$$r_D(T) \simeq \frac{1}{4T} \ , \tag{3.2}$$

which, at $T = 200$ MeV, is roughly $r_D \sim 0.25$ fm [19]. Alternatively, it can be estimated from pQCD as

$$r_D = \sqrt{\frac{1}{24\pi^2\alpha_s^2}}\frac{1}{T} \ , \tag{3.3}$$

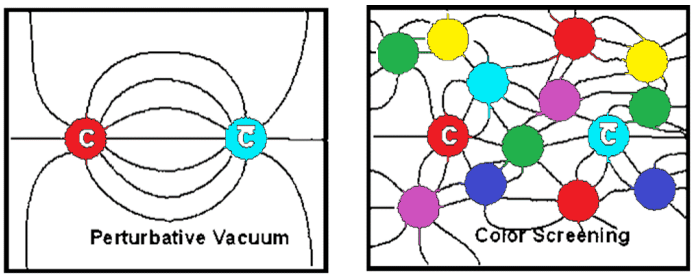

Fig. 3.2: Illustration of the dissociation of a charmonium due to the Debye colour charge screening caused by the free colour charge carriers in the deconfining medium. Based on the cartoon by T. Tveter.

which for the same temperature gives $r_D = 0.36$ fm.

3.2.1 Quarkonium potential and J/ψ suppression

As it was believed that quarkonia are created dominantly in the pre-QGP stages of the collisions—a valid assumption with the energies available at that time—suppression of the J/ψ quarkonium production was proposed in 1986 as a 'smoking gun' of the QGP creation in a famous paper by Matsui and Satz [22]. We will now show and expand on [19][6] the calculations they employed.

Quantitatively, neglecting any spin and orbit couplings, the ground state quarkonium $Q\bar{Q}$ binding potential V with the separation distance r takes the Cornell form of

$$V(r, T = 0) = \kappa r - \frac{\alpha_{\text{eff}}}{r} \ , \tag{3.4}$$

where the first term corresponds to the confining 'string-like' linear behaviour, with κ being the string tension, and the second to the Coulomb potential, with α_{eff} being the effective coulombic interaction coupling $\alpha_{\text{eff}} = \frac{4}{3}\alpha_s$. Energy of such system can be estimated from the

Hamiltonian as

$$H = \frac{p^2}{2\mu_{Q\bar{Q}}} + V(r) \tag{3.5}$$

$$\xrightarrow{\langle p^2 \rangle \sim r^{-2}} E(r) = \frac{1}{2m_Q r^2} + \kappa r - \frac{\alpha_{\text{eff}}}{r} \ , \tag{3.6}$$

where $m_Q \equiv m$ is the quark vacuum mass and $\mu_{Q\bar{Q}} = \frac{m_{Q\bar{Q}}}{2} \equiv \mu$ the reduced mass of the quarkonium system.

For the charmonia, the α_{eff} is typically taken to be $\alpha_{\text{eff}} \simeq 0.5$ [19]. This is also often used for the bottomonia, even though in principle, this value could be lower due to the shorter distance scale. Let us now estimate the value of the string tension κ. For hadrons with an internal symmetry, the total angular momentum J was found to be proportional to the square of the system energy (mass) E

$$J \sim kE^2 \tag{3.7}$$

where the slope k is experimentally found to be $k \simeq 1$ GeV^{-1} [23]. For a system of two massless quarks rotating at the speed of light on a string of radius r_0, with the local velocity of the string at $r < r_0$ being $v = \frac{r}{r_0}$, the total energy (and the total angular momentum) can be calculated by integrating the 'energy density' of the string κ (multiplied by velocity and radius resp.) along with the 'relativistic increase' from the string center to r_0 like

$$E = 2\int_0^{r_0} \frac{\kappa \, dr}{\sqrt{1 - \frac{r^2}{r_0^2}}} \qquad\qquad J = 2\int_0^{r_0} \frac{\kappa \cdot rv \, dr}{\sqrt{1 - \frac{r^2}{r_0^2}}} \tag{3.8}$$

$$= \pi\kappa r_0 \qquad\qquad = \frac{\pi}{2}\kappa r_0^2 \ . \tag{3.9}$$

This gives us $\kappa = (2\pi k)^{-1} \simeq 0.16$ GeV^{-2}.

We now search for an extremum to estimate the system size. Minimising $E(r)$ in r leads

to the following condition

$$\frac{1}{mr^3} - \frac{\alpha_{\text{eff}}}{r^2} - \kappa = 0 \ . \tag{3.10}$$

Using the values of κ and α_{eff} shown above, and the charm quark mass $m_c = 1.56$ GeV, this gives us the radius $r_{c\bar{c}} \simeq 0.20$ fm at $E = 3.1$ GeV. In vacuum, the J/ψ meson is thus smaller than a typical meson, since e.g. for pion we have $r_\pi \simeq 0.8$ fm [24].

Placing the system in a gluon heat bath of temperature T introduces two changes to the potential. First, the Coulomb infinite-range potential takes on the short-range Yukawa form. Second, the confining linear term should vanish for very high T. We will use the r_D to naively modify the potential according to our expectations, so that for $r_D \to \infty$ ($T \to 0$), we obtain the vacuum value, and for $r_D \to 0+$ ($T \to \infty$), we get no binding;

$$\begin{aligned} V(r,T) &= -\frac{\alpha_{\text{eff}}}{r}\exp(-r/r_D(T)) + \kappa r_D(T)(1 - 1 - \frac{r}{r_D(T)} - \frac{r^2}{2r_D^2(T)} - ...) \\ &= -\frac{\alpha_{\text{eff}}}{r}\exp(-r/r_D(T)) + \kappa r_D(T)[1 - \exp(-r/r_D(T))] \ . \end{aligned} \tag{3.11}$$

For different values of T, the potentials are plotted in Fig. 3.3.

For calculation's sake, let us now omit the small confining κ-term and consider only a coulombic bound state. Minimising the adequately modified $E(r)$ and setting $x \equiv r/r_D$, we obtain a following condition for the minimum

$$x(x+1)\exp(-x) = \frac{1}{m\,\alpha_{\text{eff}}\,r_D} \ . \tag{3.12}$$

The left-hand side is always positive and reaches the maximum of 0.84 at $x = 1.62$. Thus, $E(r)$ has a minimum—which means the system can be bound—only if

$$r_D > \frac{1}{0.84\,m\,\alpha_{\text{eff}}} = 1.19\,r_{\text{Bohr}} \ , \tag{3.13}$$

where $r_{\text{Bohr}} = \frac{1}{m\,\alpha_{\text{eff}}}$ is the Bohr radius of the coulombic bound system at $r_D \to \infty$, calculated

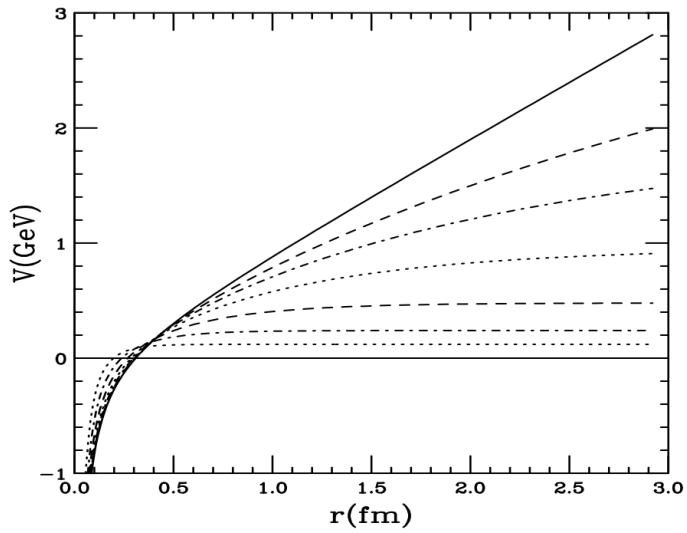

Fig. 3.3: The heavy quarkonium potential from Eq. (**??**) as function of r for different medium temperatures T. The thick solid line denotes the standard $T = 0$ potential, $r_D(T) \to \infty$, the other lines show the function for finite values of $r_D(T)$. Taken from [19].

from $E(r)$ analogously to the vacuum case shown above. In other words, the quarkonium can exist as a coulombic bound system only if the condition (3.13) holds true. For the charmonium, using the $T = 0$ value of $\alpha_{\text{eff}} \simeq 0.5$, this gives us, however, $r_{\text{Bohr}} \simeq 0.25$ fm. We see now that using the lattice value of $r_D = 0.25$ fm at $T = 200$ MeV from (3.2), the quarkonium cannot be bound in the deconfining plasma. Even for higher yet reasonable values of r_D, the dissociation is still expected, mainly because one should use a lower value of α_{eff}, which can result in a factor of two increase in the r_{Bohr}. For the bottomonia, in this simple model, we get $r^{\Upsilon}_{\text{Bohr}} = 0.08$ fm for the ground state, and thus assume it to be safe from dissociation at $T = 200$ MeV.

This suppression of the J/ψ meson, inexplicable by effects unrelated to the hot QGP phase, was indeed observed in Pb+Pb collisions at $\sqrt{s_{\text{NN}}} = 158$ GeV with the NA50 experiment. A ratio of the measured J/ψ yield and the expected yield, obtained by extrapolating p+A results including cold nuclear matter effects to A+A conditions, is shown in Fig. 3.4.

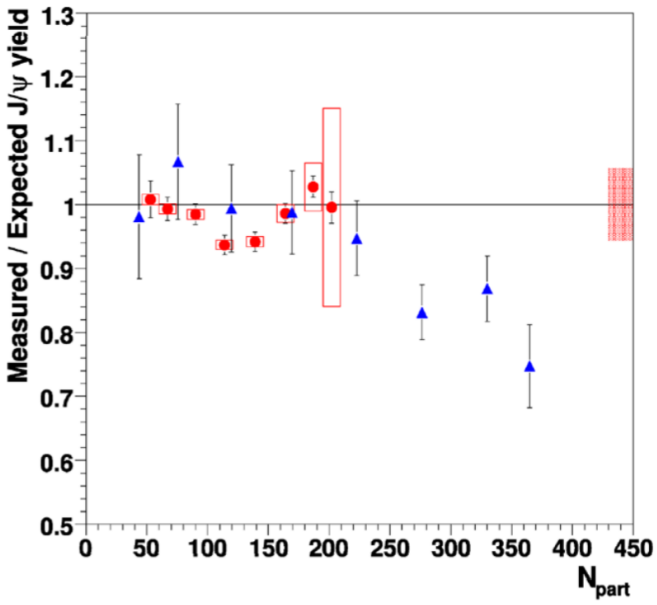

Fig. 3.4: Ratio of the observed and expected (scaled proton-nucleus) yield of J/ψ in Pb+Pb collisions at $\sqrt{s_{\mathrm{NN}}} = 158$ GeV as measured with the NA50 experiment, showing an anomalous suppression. Taken from [25].

3.2.2 Sequential melting – QGP thermometer

For a given quarkonium state, the described dissociation mechanism depends on two things: the medium temperature and the quarkonium radius, which is related to the binding energy. Thus, states of different binding energies are expected to 'sequentially melt' at different medium temperatures. This behaviour has been proposed as a 'QGP thermometer'—by measuring which quarkonium states were suppressed by colour screening and which not, one can infer constraints on the plasma temperature [26].

This sequential suppression pattern is illustrated in Fig. 3.5 (*left*), which shows what states are expected to survive at given temperature. Net suppression of the quarkonium production for various states measured by CMS at $\sqrt{s_{\mathrm{NN}}} = 2.76$ TeV is shown in Fig. 3.5 (*right*). There, it can be seen that the higher binding energy states (J/ψ, $\Upsilon(1S)$) are significantly less suppressed than the lower binding energy ones ($\psi(2S)$, $\Upsilon(2S)$, $\Upsilon(3S)$).

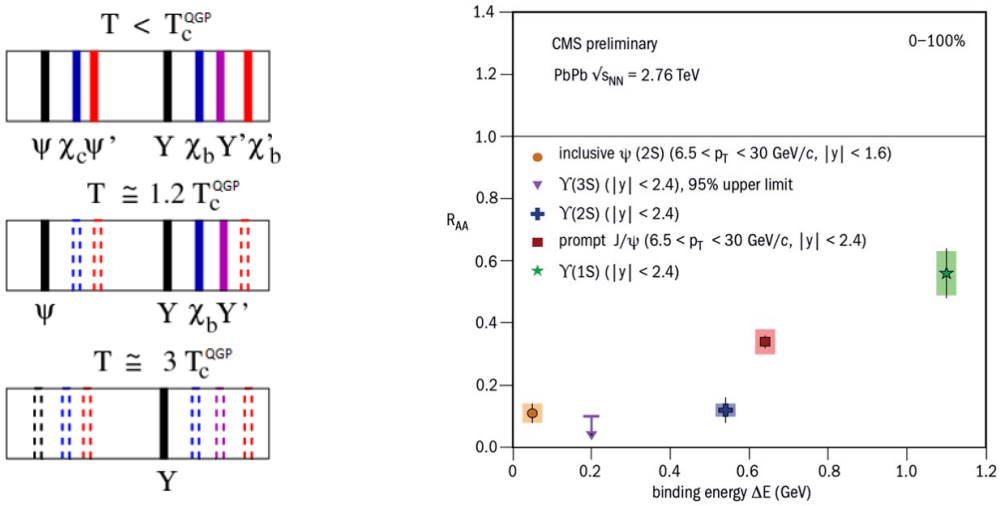

Fig. 3.5: *(left)* Diagram of the sequential melting expectation, showing which quarkonium states survive at given T. *(right)* Comparison of the measured suppression for different quarkonium states with the CMS experiment. Taken from [27][28].

3.3 Statistical recombination

Studying the dependence of the measured suppression on the collision energy brings up a rather surprising fact. Fig. 3.6 (*left*) shows the R_{AA} of J/ψ at the LHC ($\sqrt{s_{\mathrm{NN}}} = 2.76$ TeV) and RHIC ($\sqrt{s_{\mathrm{NN}}} = 0.2$ TeV). Despite the collision energy being by a factor of 10 larger, at the LHC, the J/ψ is much less suppressed ($R_{AA} \sim 0.6$ at LHC vs $R_{AA} \sim 0.2$ at RHIC in the most central collisions). This is counter-intuitive because we would expect that the colour screening effect would be more prominent with higher T.

A relatively simple explanation to this conundrum emerges when one looks at the charm quark cross-section as a function of the system collision energy, which is plotted in Fig. 3.7 (*right*). Although the uncertainties of the calculations are still significant, on average, this gives us ~ 100 $c\bar{c}$ quark pairs per event at the LHC and only ~ 10 $c\bar{c}$ quark pairs per event at RHIC. Therefore, at the LHC, the charm quarks are abundant enough for the J/ψ to be secondarily produced by the coalescence at the QGP phase boundary. This 'statistical recombination' regenerates the suppression by the colour screening and, in principle, should the collision

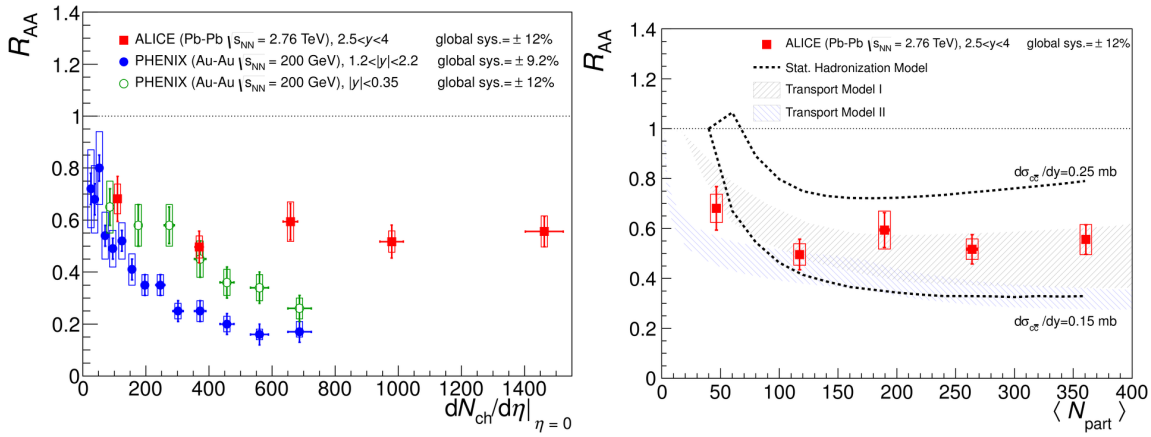

Fig. 3.6: Nuclear modification factor for J/ψ as a function of multiplicity (*left*) and mean number of participants (*right*). Results from RHIC are also shown in the left plot. Taken from [29].

energy be high enough, can even enhance the production. See Fig. 3.7 (*left*) for a cartoon illustrating this behaviour.

Statistical models taking into account the recombination can successfully describe the measured R_{AA}, as can be seen in Fig. 3.6 (*right*). Further evidence supporting the fact that, at the LHC, a significant fraction of the J/ψ comes from the plasma coalescence can be found in the non-zero magnitude of the elliptic flow of the J/ψ. At RHIC, however, the v_2 is consistent with zero. This is displayed in Fig. 3.8 and hints at the fact that at RHIC energies, the secondary production is not so prominent.

3.4 Cold nuclear matter effects

Apart from the recombination, further effects complicate the interpretation of the measured suppression. There are other behaviour emergent in nuclear collisions—unrelated, however, to the hot QGP phase—which affect the total production. Although this is not always the case in the community, in this work, we will collectively call *all* of these the 'cold nuclear matter effects' (CNM). They are generally studied in p+A collisions, where they should still play a role, although the QGP creation is not expected. We will now explain some of the

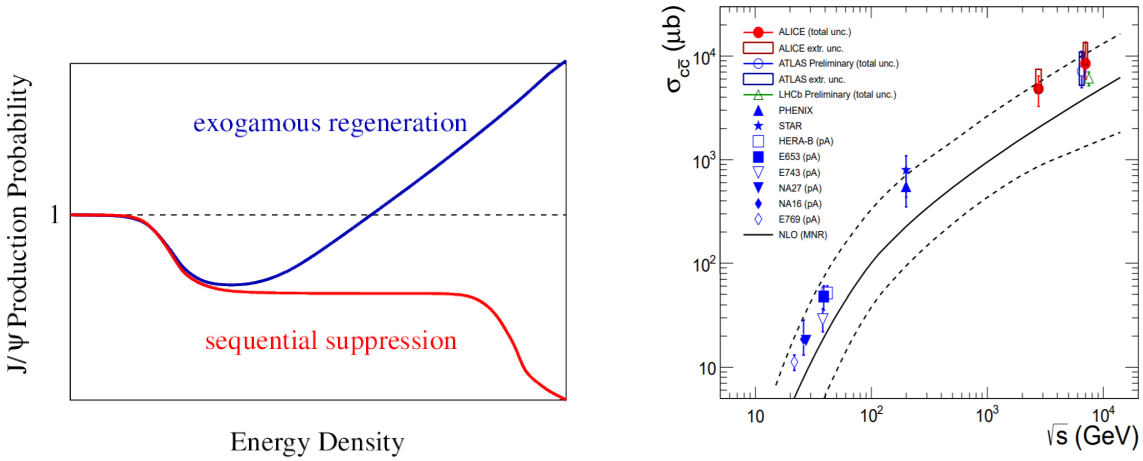

Fig. 3.7: (*left*) Diagram depicting the different effects of regeneration and sequential melting on the J/ψ production. (*right*) Production cross-section of the $c\bar{c}$ pair as a function of system energy. Taken from [30][31].

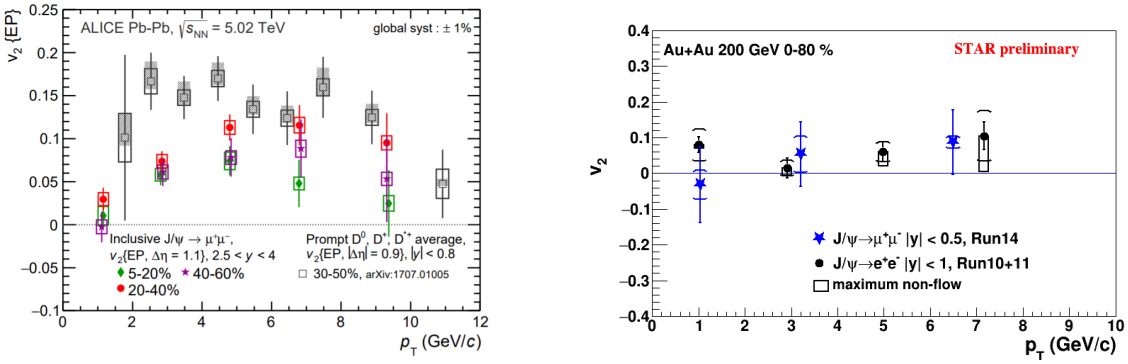

Fig. 3.8: Elliptic flow of the J/ψ as a function of transverse momentum at the LHC (*left*) and RHIC (*right*). Taken from [32][33].

notable CNM effects.

3.4.1 Nuclear shadowing

In accelerated, heavily Lorentz-contracted nuclei, the nucleons' partonic densities are different from those in single protons/neutrons in order to not violate the uncertainty principle. Understandably, this modifies any subsequent production that takes place in the earliest stages of the collision. Since heavy quarks come dominantly from gluons, let us now focus on those.

One usually factorises the nuclear partonic distribution function (nPDF) $F_g^A(x_1, \mu_f)$ as a product of the single nucleon partonic distribution function (PDF) $g(x_1, \mu_f)$ and the shadowing ratio $R_g^A(x_1, \mu_f)$:

$$F_g^A(x_1, \mu_f) = g(x_1, \mu_f) \times R_g^A(x, \mu_f) \ , \tag{3.14}$$

where x is the Björken momentum-fraction and μ_F the adequate factorisation scale [34]. An example of the gluon PDF's and the shadowing ratios—at the scales typically used to calculate the J/ψ and $\Upsilon(1S)$ production ($\mu_F \sim m_{\mathrm{T}}$)—can be found in Fig. 3.9 and Fig. 3.10 respectively.

Production of a quarkonium state C in p+A collisions, taking into account the shadowing effect, is then calculable via the factorisation theorem [34]

$$\frac{\sigma_{pA\to C}}{dy\, dp_{\mathrm{T}}\, d\vec{b}} = \int dx_1\, dx_2\, J\, g(x_1, \mu_f) F_g^A(x_2, \vec{b}, \mu_f)\, \frac{d\sigma_{gg\to Cg}}{d\hat{t}} \ , \tag{3.15}$$

where J is the Jacobian and $\frac{d\sigma_{gg\to Cg}}{d\hat{t}}$ the C-state production cross section, calculable e.g. from the CEM model. Looking back at the Fig. 3.10, we see that based on the x of the nuclear parton, the effect on the production can differ. For the J/ψ, there is a suppression from $x < 10^{-2}$ and an enhancement at $10^{-2} < x < 10^{-1}$ (called 'anti-shadowing'). For the $\Upsilon(1S)$, the shadowing effect is slightly less pronounced.

Fig. 3.11 shows the R_{AA} of the J/ψ in p+Pb collisions at $\sqrt{s_{\mathrm{NN}}} = 5.02$ TeV. The positive

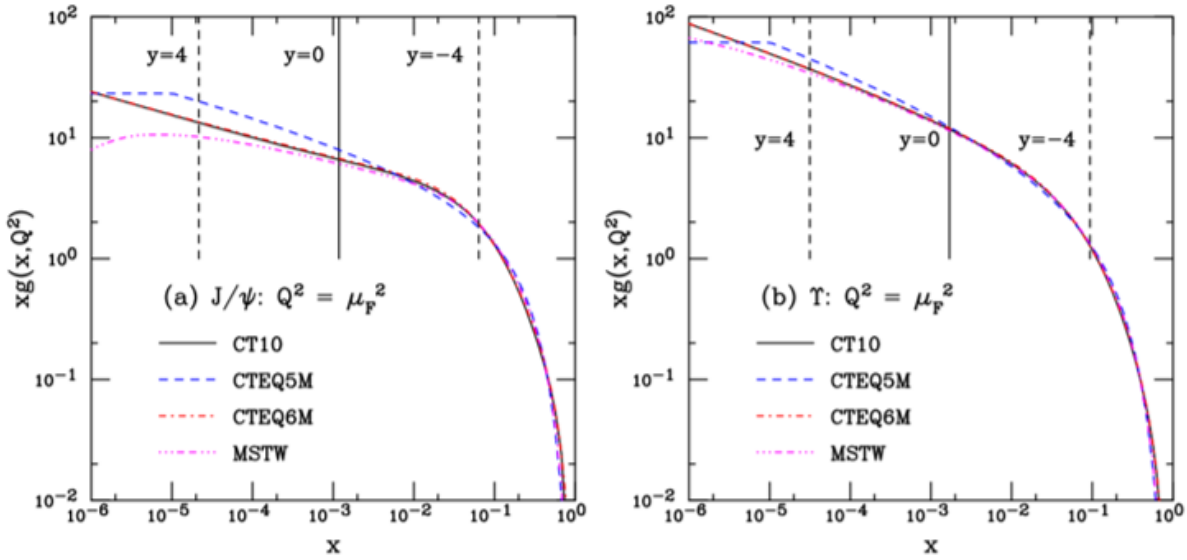

Fig. 3.9: Gluon densities in a nucleon at scales for the J/ψ (*left*) and $\Upsilon(1S)$ (*right*) production. Taken from [34].

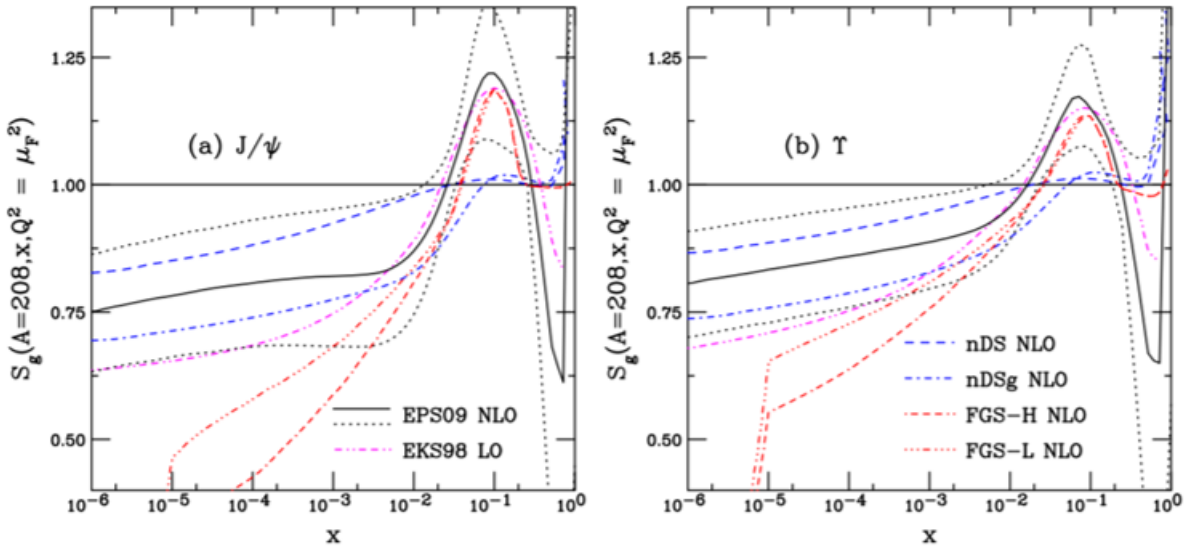

Fig. 3.10: Gluon shadowing ratios for Pb nuclei with the factorisation scales for J/ψ (*left*) and $\Upsilon(1S)$ (*right*). Taken from [34].

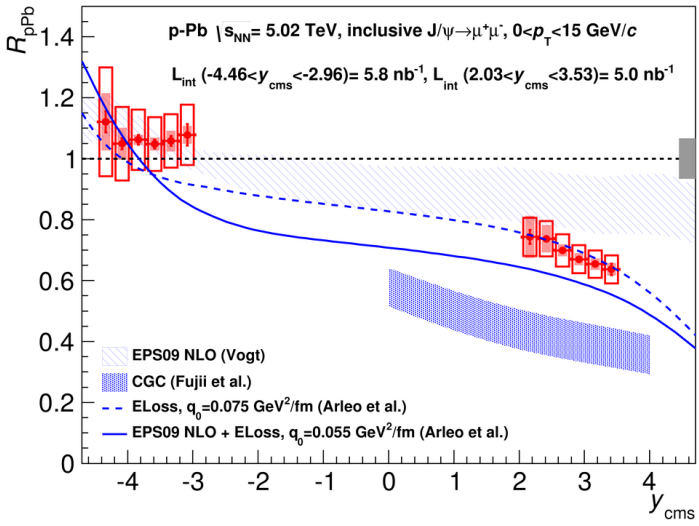

Fig. 3.11: Nuclear modification factor for J/ψ in p+Pb collisions at $\sqrt{s_{\rm NN}} = 5.02$ TeV as a function of centre-of-mass rapidity from the ALICE collaboration. Positive rapidity is defined in the proton-going direction. Taken from [36].

rapidity is defined in the proton-going direction. In this result, we observe that the J/ψ is suppressed at $y > 0$, although at $y < 0$, there are even hints of enhancement. We can now relate the rapidity regions to x via

$$x_{1,2} = \frac{m_T}{\sqrt{s_{\rm NN}}} \exp(\pm y) \ . \tag{3.16}$$

At the very forward or backward rapidities of $y \sim +(-)3$, we thus access regions of $x_2 \sim 10^{-5}$ or $x_2 \sim 10^{-1}$–10^{-2}. Juxtaposing this with the shadowing ratios, we indeed see that the former case corresponds to the large shadowing region, whereas the latter just about borders with the anti-shadowing regime. As is also apparent from the plot, results using the nPDF's together with models taking into account initial state parton energy loss can accurately describe the measured y-dependence of the R_{AA}. Such 'energy loss' is expected to be caused by the multiple rescattering of the interacting partons on the partonic cloud of the nucleus, usually resulting in the broadening of the $p_{\rm T}$-spectra (Cronin effect) [35].

3.4.2 Quarkonium suppression by hadrons

We have explained how can the difference in the initial conditions in nuclear collision result in the observed suppression of the quarkonia. If this was the only effect, however, one would expect the same suppression for all of the states of the given family. This is due to causality—there cannot be any discrimination for the production of the pre-quarkonium constituents based on what final state are they going to evolve into. In simpler words, the constituents 'don't know' whether they will end up as a J/ψ or $\psi(2S)$, for instance. That being said, however, we see a clear difference in the suppression of those two states in p+A collisions, as is shown in Fig. 3.13 (*left*). This implies the presence of other medium-related phenomena, which would be present for a sufficiently long time after the collision.

At SPS energies, this has been identified with the absorption by passing-by nuclear remnants, the so-called 'nuclear break-up'. Larger nuclei result in larger path length L (calculable from Glauber), which would in turn mean higher probability for absorption. Fig. 3.12 shows the measured J/ψ cross-section in collisions of: Be, Al, Cu, In, Pb, and U. A clear suppression, rising with L, is observed. This is usually parametrised as

$$\sigma_{AA\to C} = A^2\,\sigma_{pp\to C} \times \exp(-L\,\rho_N\,\sigma_{\text{abs}})\ , \tag{3.17}$$

where $\sigma_{AA\to C}$ and $\sigma_{pp\to C}$ are the cross-sections for the quarkonium state C in A+A or p+p collisions resp., $\rho_N \simeq 0.14$ fm^{-3} the nuclear density, and σ_{abs} the effective absorption of the state C by a nucleus. For the J/ψ, calculations predict $\sigma_{\text{abs}}^{J/\psi} \sim 5$ mb [6] at the SPS energies, whereas for the $\Upsilon(1S)$, values of $\sigma_{\text{abs}}^{\Upsilon(1S)} \sim 2$ mb $\approx (\frac{r_{\Upsilon(1S)}}{r_{J/\psi}})^2\,\sigma_{\text{abs}}^{J/\psi}$ are typically used [18].

At LHC energies, however, this mechanism is insufficient to explain the different suppression between the ground state and the excited charmonia. The formation time of the quarkonium state in the rest frame of the nucleus is $t_f = \gamma\tau_f$, where τ_f is the proper formation time, which can be estimated from the uncertainty relations $\frac{1}{\Delta m} \sim 10^{-1}$ fm. The boost factor can be obtained from the quark-pair and the beam rapidity $\gamma = \cosh(y - y_{\text{beam}})$, where $y_{\text{beam}} = -\log(\frac{\sqrt{s_{\text{NN}}}}{m_N}) \simeq -5.4$ at RHIC or $y_{\text{beam}} \simeq -8.1$ at the LHC [38]. At RHIC mid-

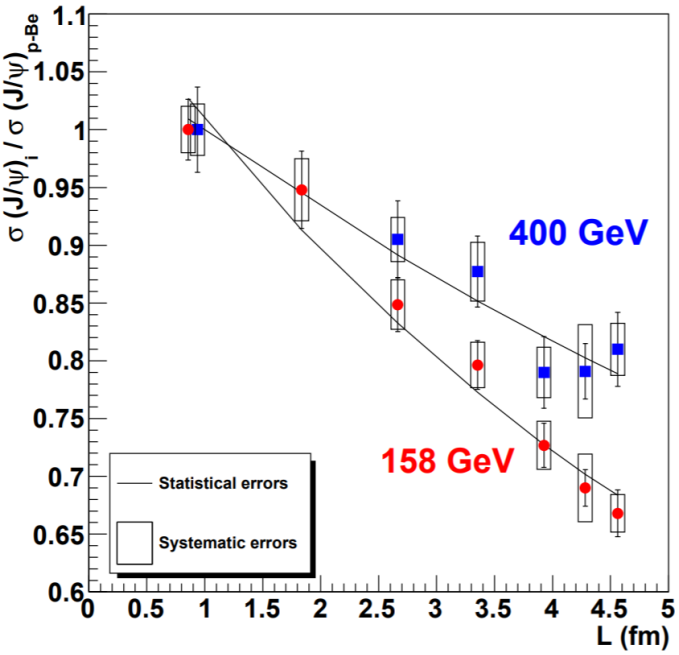

Fig. 3.12: Ratios of the J/ψ production cross section in collisions of different nuclei w.r.t. beryllium at $\sqrt{s_{\mathrm{NN}}} = 158$ GeV and $\sqrt{s_{\mathrm{NN}}} = 400$ GeV as a function of mean path length. The different datapoints correspond to collisions of: Be, Al, Cu, In, W, Pb, U. Taken from [37].

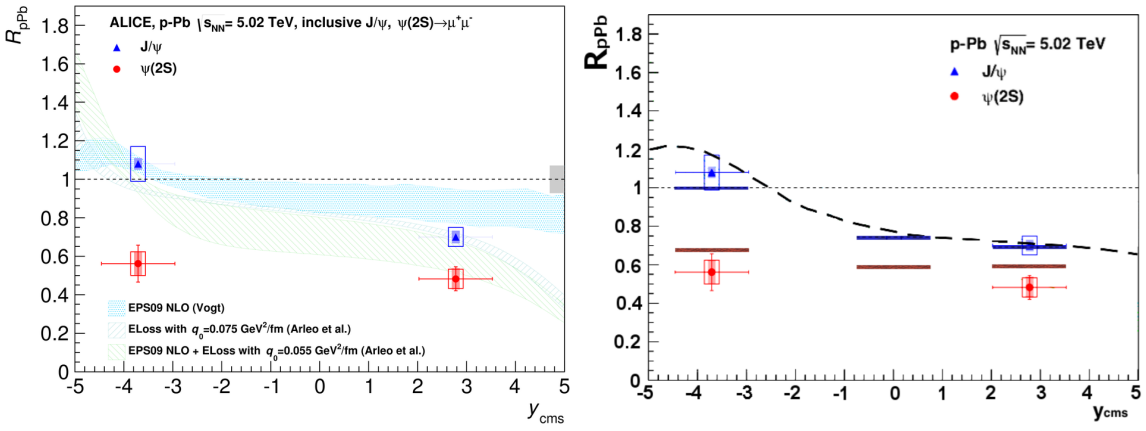

Fig. 3.13: Nuclear modification factor for J/ψ and $\psi(2S)$ in p+Pb collisions at $\sqrt{s_{\rm NN}} = 5.02$ TeV by the ALICE collaboration. Comparison with models including shadowing (*left*) and shadowing+co-mover absorption (*right*) is also shown. Taken from [39][38].

and forward rapidity, this gives $\gamma > 100$ and thus $t_f >> r_{\rm Au} \sim 10$ fm. At the LHC, this is even more prominent, with $\gamma > 1000$. This means that by the time the charmonium state forms, the nucleus is long gone and thus, nuclear absorption cannot explain the different suppression, which is present at forward rapidity. In the very backward rapidity at the LHC ($\gamma \approx 30$), t_f can be on the same order of magnitude as $r_{\rm Pb}$, this, however, still cannot account for the factor of two smaller R_{AA} [38].

Previous comments suggest that there must be other medium effects in p+A collisions, acting over sufficiently long time so that different states can be distinguished. A popular method to explain this is by including the possibility of inelastic interactions with secondary hadrons in near phase space, the so-called absorption by co-movers.

The survival probability $S_C^{co.}$ of a quarkonium C in the co-movers' presence can be found by integrating the kinetic rate equation

$$\tau \frac{d\rho^C}{d\tau}(b,r,y) = \sigma^{co.-C}\,\rho^{co.}(b,r,y)\,\rho^C(b,r,y) \tag{3.18}$$

$$\xrightarrow{\int_{\tau_0}^{\tau_f}} S_C^{co.}(b,r,y) = \exp(-\sigma^{co.-C}\,\rho^{co.}(b,r,y)\,\log\frac{\tau_f}{\tau_0})\ , \tag{3.19}$$

where ρ^C and $\rho^{co.}$ are the densities of C or co-movers resp. at a given impact parameter b,

transverse distance r, and rapidity y, $\sigma^{co.-C}$ the inelastic cross-section between the co-moving hadron (pion) and C, and the integration is from a certain initial time τ_0 to kinetic freeze-out time τ_f [38]. Multiplying calculated values of $\sigma_{pA\to C}$ (which include shadowing) with $S_C^{co.}$ gives for R_{pA} that can rather accurately describe data, as can be seen in Fig. 3.13 (*right*).

Chapter 4

Experimental setup

This chapter provides an overview of the experimental facility used in the acquisition of the data for the analysis presented in this thesis. In the first part, the accelerator is presented. Subsequently, the detector and its notable sub-systems are described.

4.1 The RHIC accelerator facility

The Relativistic Heavy Ion Collider is a heavy-ion accelerator located at the Brookhaven National Laboratory (BNL) in New York, USA. The RHIC facility and its experiments have been essential in the investigation of heavy-ion collisions and searches for the QGP. The ions are accelerated in two separate storage rings, which intersect at six interaction points. As of now, only one of the points is used—by the STAR experiment. In the past, however, the PHENIX, PHOBOS, and BRAHMS experiments were present, all of which have completed their data-taking.

At RHIC, heavy ions can be accelerated up to $\sqrt{s_{\mathrm{NN}}} = 200$ GeV. Thanks to its ion source, various ions can be accelerated—besides the normally used gold, collisions of nuclei of, for instance, uranium or copper have also been measured. Another important feature is the option to change the collision energy of the ions. This was utilised in the Beam Energy Scan (BES) programme, which is important in studying the QCD phase diagram. Furthermore,

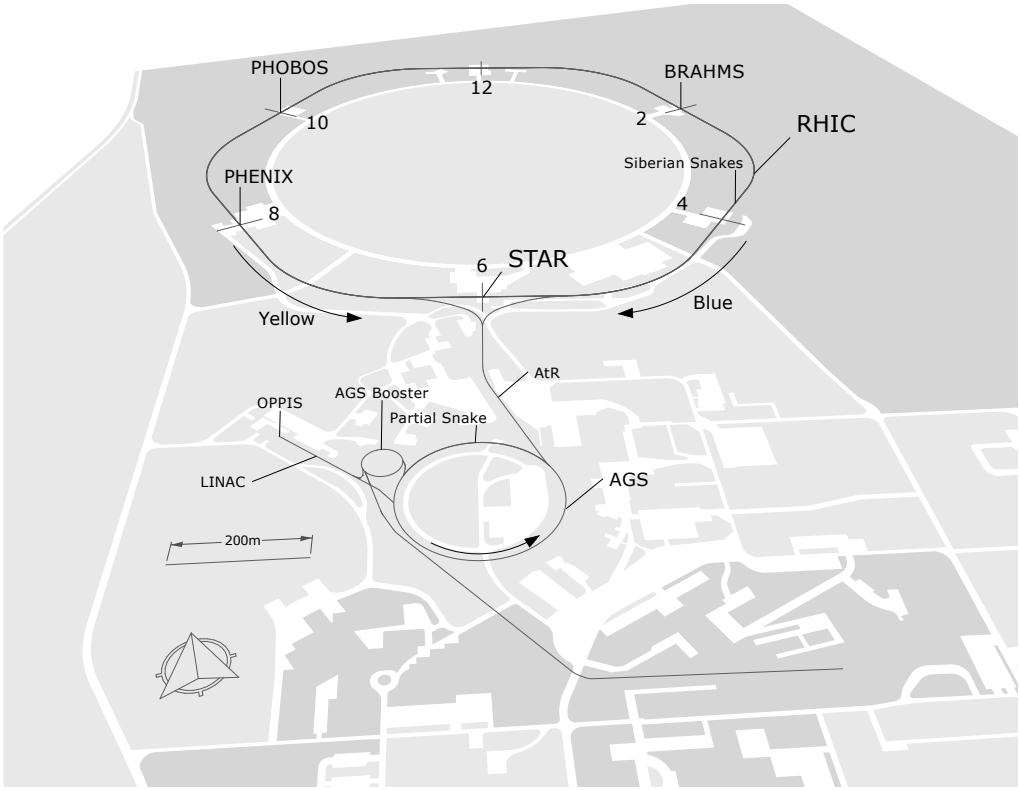

Fig. 4.1: Depiction of the RHIC accelerator complex. Taken from [41].

proton beams can be collided. These can be polarised, which makes RHIC the most powerful polarised proton beam accelerator in the world.

The layout of the accelerator complex can be seen in Fig. 4.1. For detailed information on the accelerating procedure and beam characteristics, refer to [40].

4.2 The STAR experiment

The Solenoidal Tracker At RHIC is a multi-purpose heavy-ion collisions detector with full coverage in azimuth ($0 < \varphi < 2\pi$) at mid-rapidity ($|\eta| < 1$). Thanks to its excellent PID capabilities and constant upgrades, STAR belongs to the world's leading heavy-ion experiments. Majority of the detector is surrounded by a solenoidal magnet system, which subjects it to a magnetic field of 0.5 T, parallel to the beam-line. The STAR experiment can be seen in Fig. 4.2. Some of its most prominent sub-systems are:

- Time Projection Chamber (TPC),
- Barrel Electromagnetic Calorimeter (BEMC),
- Time Of Flight detector (TOF): greatly improves PID capabilities for particles with momentum up to 3 GeV/c by measuring their velocity β,
- Muon Telescope Detector (MTD): located behind the magnet, this detector provides PID and a trigger for muons,
- Heavy Flavor Tracker (HFT): a silicon detector placed as close as 2.5 cm from the beam-pipe, which improves secondary vertex resolution up to ~ 40 μm,
- Vertex Position Detector (VPD): a quick coincidental detector used for triggering and on-line determination of a primary vertex position.

The two detectors most relevant to the presented measurements—the TPC and the BEMC—are described in more detail further in the chapter.

4.2.1 Time Projection Chamber

The TPC [42] is the primary tracking detector within STAR. This 4.2 m long cylinder with 2 m outer radius is also responsible for primary vertex reconstruction and provides PID via ionisation energy loss dE/dx. The chamber is filled with a mixture of argon (90%) and methane (10%) and operated 2 mbar above the atmospheric pressure. A thin high voltage membrane of -28 kV is situated at $z = 0$ and together with grounded end-caps provides a homogeneous electric field of 135 V/cm. This field causes the electrons from the ionisation to drift at a constant velocity of 5.5 cm/μs, which results in the maximum drift time of ~ 40 μs. The detector is illustrated in Fig. 4.3.

The electrons are collected and read-out at the end-caps via the Multi-Wire Proportional Chambers (MWPCs). They are divided into 12 sectors and each of these holds 45 pad-rows, 13 in the inner region and 32 in the outer. The inner region has continuous pad coverage

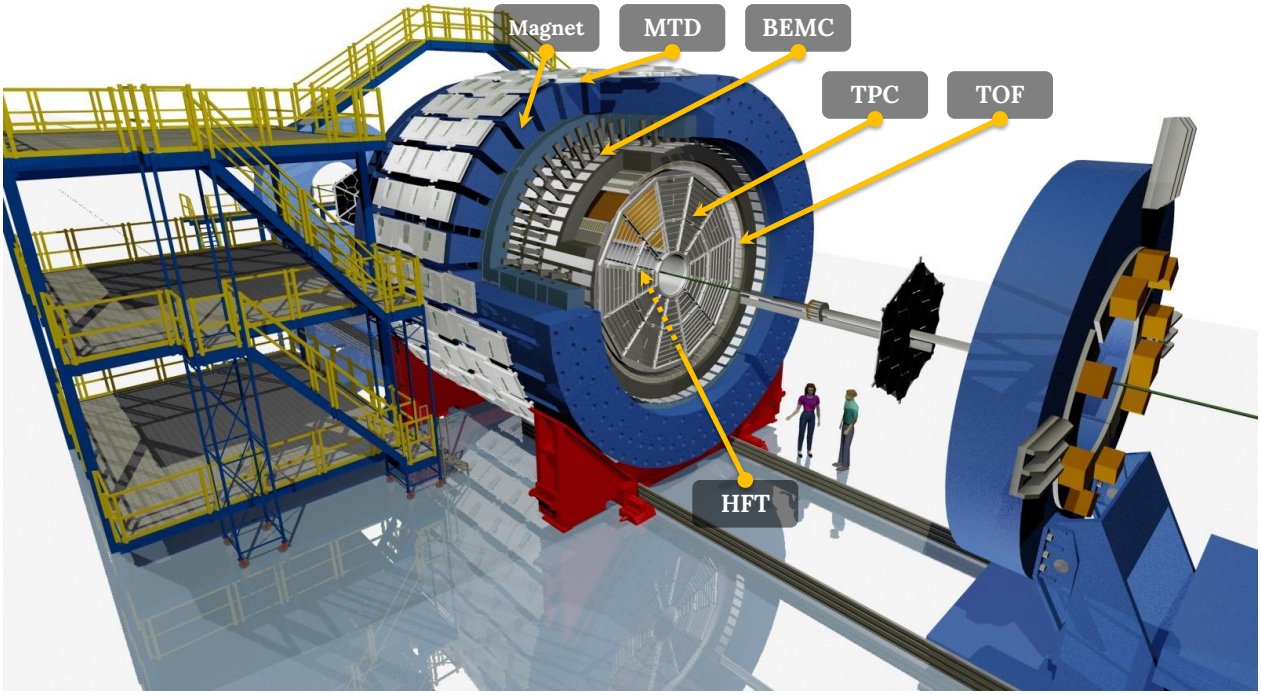

Fig. 4.2: Illustration of the STAR detector and some of its subsystems. Reproduced from [41].

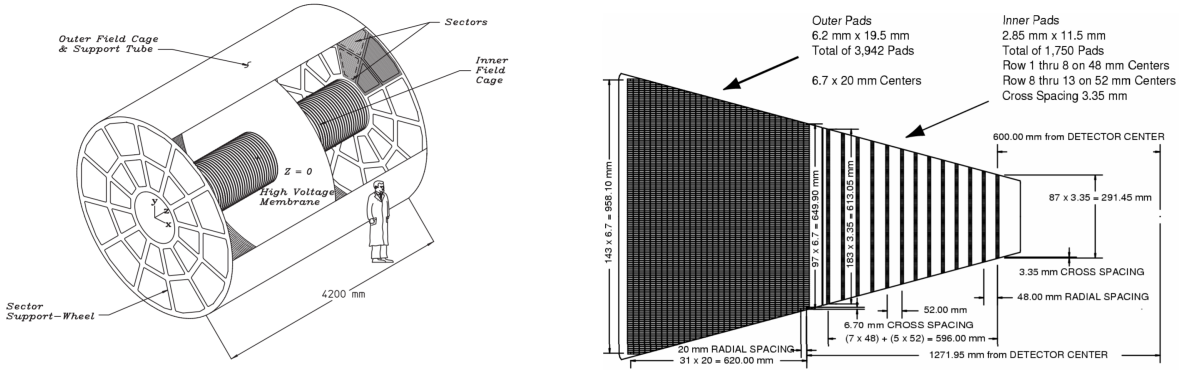

Fig. 4.3: Picture of the TPC detector (*left*); one of the end-cap MWPC sectors (*right*). Taken from [42].

to facilitate the $\mathrm{d}E/\mathrm{d}x$ measurement. The inner region has smaller pads to provide a better resolution for the higher track densities. The sector and its parameters can be seen in Fig. 4.3.

The TPC is also used to help identify particle species. This is done by constraining the variable $n\sigma_i$, which is defined as follows,

$$n\sigma_i = \log \frac{dE/dx}{\langle dE/dx \rangle_i} \ , \tag{4.1}$$

where $\langle dE/dx \rangle_i$ is the characteristic mean energy loss for a particle species i, predicted by Bichsel functions. Distribution of dE/dx along with the characteristic value, i.e. $n\sigma_i = 0$,is plotted in Fig. 4.4.

4.2.2 Barrel Electromagnetic Calorimeter

The BEMC [43] is a fast sampling calorimeter system situated behind the TPC and the TOF detectors, sharing their azimuthal and pseudorapidity coverage. It is used for triggering, detection of photons, and PID of mainly electrons via E/p. The trigger operates on a high-tower principle, with a three-level customisable threshold (labelled as BHT1, BHT2, and BHT3). The trigger is fired if a bit-shifted value of ADC exceeds the given threshold.

The barrel's inner radius is ~ 2.2 m and its outer radius ~ 2.5 m. The detector consists of 120 modules, each holding 2×20 cells—the towers. One tower has a coverage of $\Delta\varphi \times \Delta\eta \simeq 0.05 \times 0.05$. They are composed of 21 scintillator tiles (created by light-insulating the module 'megatiles' tower-by-tower), interleaved with 20 lead absorber plates. Cells of the Barrel Shower Maximum Detector (BSMD)—which improves the spatial and shape resolution of the produced shower—are situated between the fifth and the sixth layer. Light from the scintillator tiles are collected by means of Wavelength Shifting Fibres (WLS), connecting to clear optical fibres, and then read-out by Photo-Multiplier Tubes (PMT). The geometry of the BMC and its modules, as well as a layout of BEMC towers, is displayed in Fig. 4.5.

The BEMC is also utilised to help identify the electrons. This is due to the fact that, unlike charged hadrons, electrons are expected to lose all of their energy in the calorimeter.

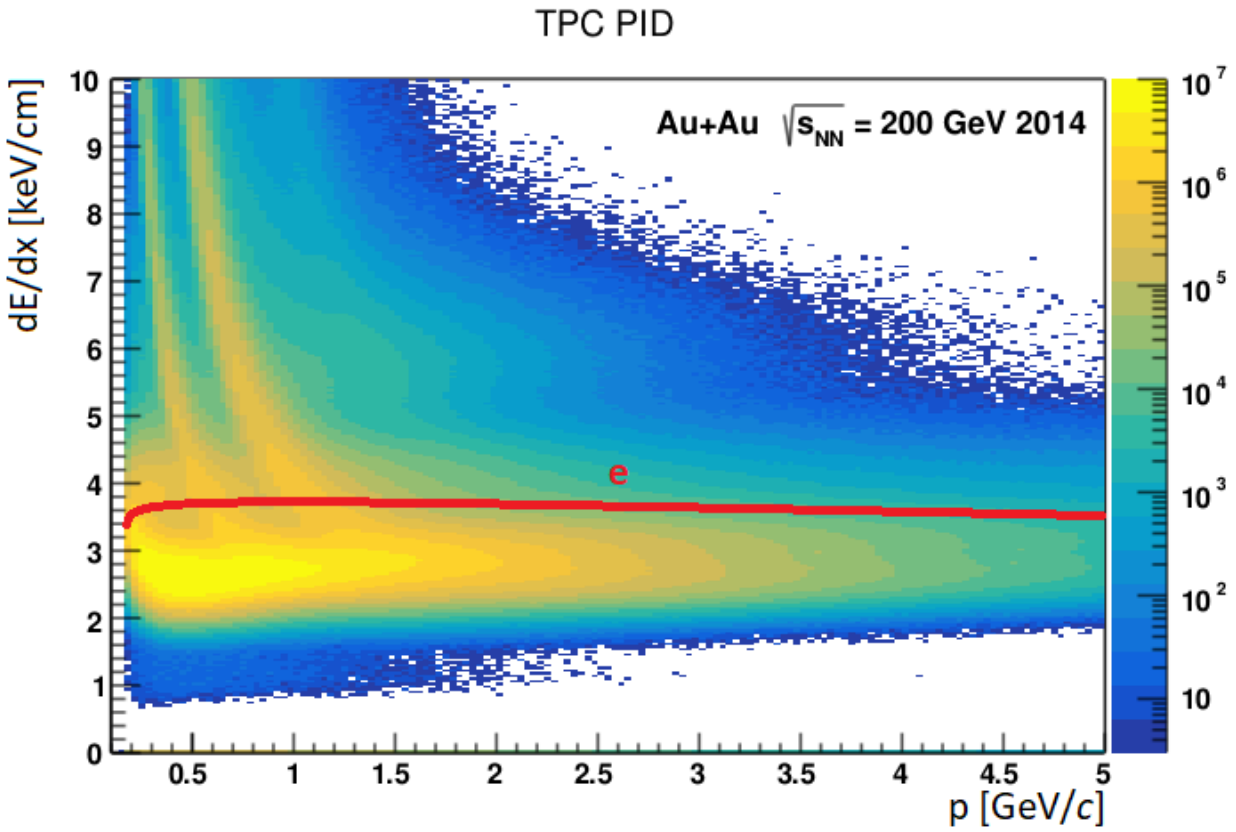

Fig. 4.4: *THIS ANALYSIS*: (*left*) Distribution of the TPC tracks energy loss $\mathrm{d}E/\mathrm{d}x$ vs. primary momentum p. The notable yellow structures in the $\mathrm{d}E/\mathrm{d}x$ plot belong to the pions, electrons, kaons, and protons, going from bottom left to top right. The typical energy loss for electrons is showed as a red line.

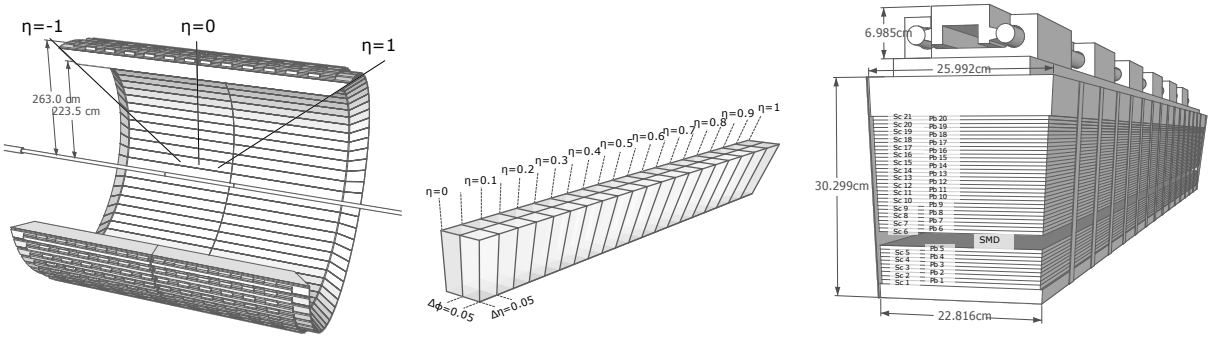

Fig. 4.5: Illustration of the STAR BEMC detector (*left*); a BEMC module geometry (*middle*); layout of BEMC towers (*left*). Taken from [41] [43].

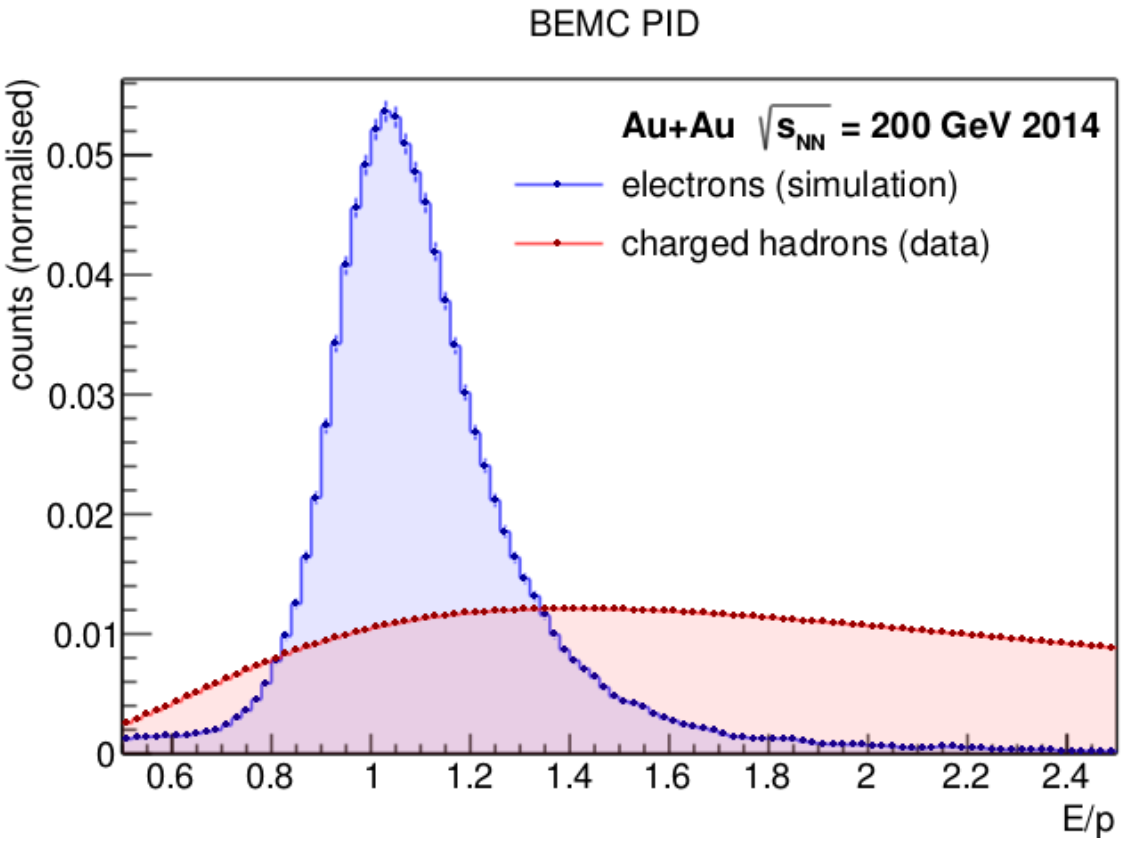

Fig. 4.6: *THIS ANALYSIS*: (*left*) Distribution of the E/p ratio for electrons (determined from simulations) and of all charged hadrons (measured in real data). The distributions are both normalised to unity.

Therefore, constraints on the E/p ratio can be imposed. The different distributions of E/p for electrons and charged hadrons are shown in Fig. 4.6.

Chapter 5

Author's analysis on $\Upsilon \to e^+e^-$

This chapter is the principal part of this thesis and overviews the author's analysis on the Υ meson production using the di-electron channel. Measuring the Υ at RHIC energies has the advantages of virtually no regeneration [18] and smaller effect of certain CNM phenomena, such as the break-up by co-movers [53].

5.1 Dataset and tools

This analysis has been carried out on the data collected in 2014 with the STAR experiment from Au+Au collisions at $\sqrt{s_{\mathrm{NN}}} = 200$ GeV. Since the Υ production is very scarce[1], the BHT2 trigger (see Chapter 4) was used in the data collection.

The analysed data are in the format of *picoDST* (reduced Data Storage Tree), created in *root4star*, which is a version of the ROOT framework [44] customised for the STAR collaboration. The ROOT framework is an analysis software structure designed for effective evaluation of large-scale data in particle physics. It is written in the C++ programming language.

The total data sample consisted of two sub-datasets, referred to as *lowmid* and *high*. They correspond to two distinct data productions, one configurated for low- and mid-luminosity of

[1] In p+p collisions, there is only one $\Upsilon(1S)$ produced per approximately 10^6 minimum-bias events, and just $\sim 0.1\%$ of these are successfully reconstructed in the di-electron channel.

Collision system, energy	Au+Au $\sqrt{s_{\mathrm{NN}}} = 200$ GeV	Run year	2014
Trigger	BHT2*VPDMB-30	picoDST production tag	P15ic
Number of events	114.2M	*lowmid*-dataset fraction	45.7%
Integrated luminosity	3.96 nb^{-1}	*high*-dataset fraction	54.3%

Tab. 5.1: A summary of the dataset used for the analysis. The listed fractions represent fractions of the total luminosity.

the beam, the second for high-luminosity. They differ slightly, mainly in the tracking. The *picoDST*'s of Run 14 held over one billion events, vast majority of which were minimum-bias events and unused in this analysis. A total of 114.2M good BHT2-triggered events were selected from this, which corresponds to the integrated luminosity of ~ 3.96 nb^{-1}. A summary of the dataset can be found in Tab. 5.1.

5.1.1 Event selection

The following set of quality cuts was applied on the events:

- $|v_z^{\mathrm{TPC}}| < 30$ cm; the z-coordinate of the TPC-reconstructed primary vertex of the event,
- $|v_z^{\mathrm{TPC}} - v_z^{\mathrm{VPD}}| < 4$ cm; the difference between z-coordinates of the TPC-reconstructed and VPD-measured primary vertices,
- the event is BHT2-triggered.

Distributions of the inclusive events' v_z^{TPC} and v_z^{VPD} with the applied cuts are plotted in Fig. 5.1.

5.1.2 Event centrality

At STAR, centrality is calculated from the reference multiplicity *grefMult*, which is the number of charged particles at $|\eta| < 0.5$ and with the distance of closest approach (DCA) to the primary vertex DCA<3 cm. The *grefMult*, however, needs to be corrected to account for run-dependent TPC irregularities, which is done on the basis of run-by-run studies of

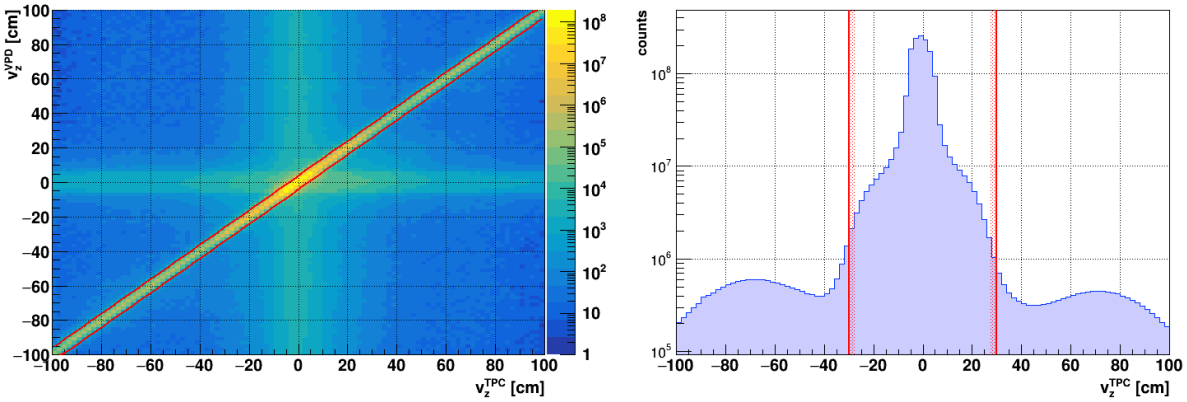

Fig. 5.1: *THIS ANALYSIS*: Distributions of the z-coordinate of the primary vertex v_z^{TPC} vs. the v_z^{VPD} (*left*) and the v_z^{TPC} (*right*). The red lines denote the applied cuts.

events. The *grefMult* is then related to the centrality classes via comparison with Glauber-model expectations. A centrality class of eg. 0–10% corresponds to the 0–10% most central collisions.

Distributions of the corrected and uncorrected multiplicities as well as the centrality classes for the selected events can be seen in Fig. 5.2. It is noteworthy that the centrality distribution is not uniform, which is seemingly inconsistent with the definition of the classes. This, however, comes from using the BHT2-triggered events, which are generally biased towards more central collisions.

5.2 Upsilon reconstruction

This analysis utilises the di-electron decay channel of the Υ, although reconstruction via di-muons is also possible thanks to the installation of MTD in 2014. The electrons are identified with a combination of TPC and BEMC. A TPC-reconstructed primary track must be successfully matched to a cluster within BEMC. A BEMC cluster is defined as a collection of three neighbouring BEMC towers with the highest energy deposit. At least one of the two electron daughters must also be matched to the tower which fired the BHT2 trigger. A simple cartoon of the reconstruction is shown in Fig. 5.3.

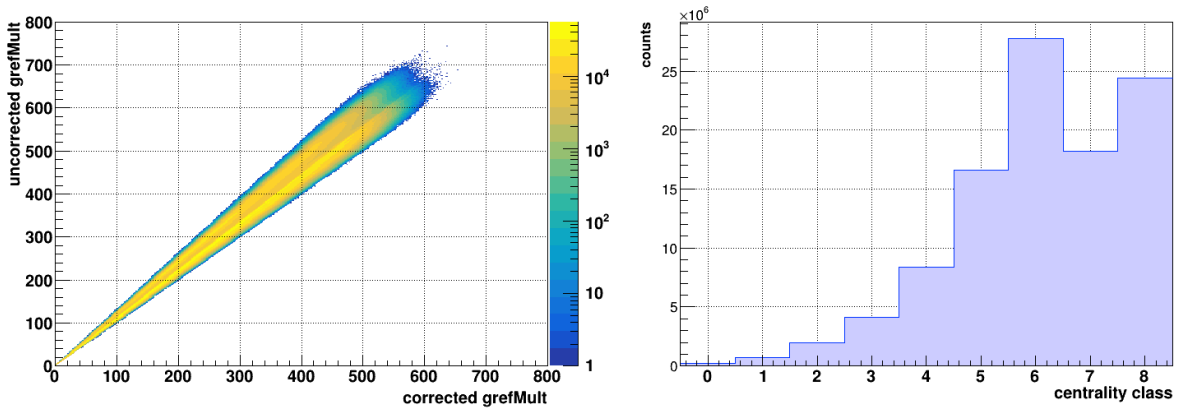

Fig. 5.2: *THIS ANALYSIS*: (*left*) Distribution of the corrected vs. the uncorrected *grefMult* charged-tracks multiplicity. (*right*) Distribution of the centrality classes. The class 8 corresponds to 0–5% of the most central collisions, class 7 to 5–10%, class 6 to 10–20%, and further on, with an increment of 10%.

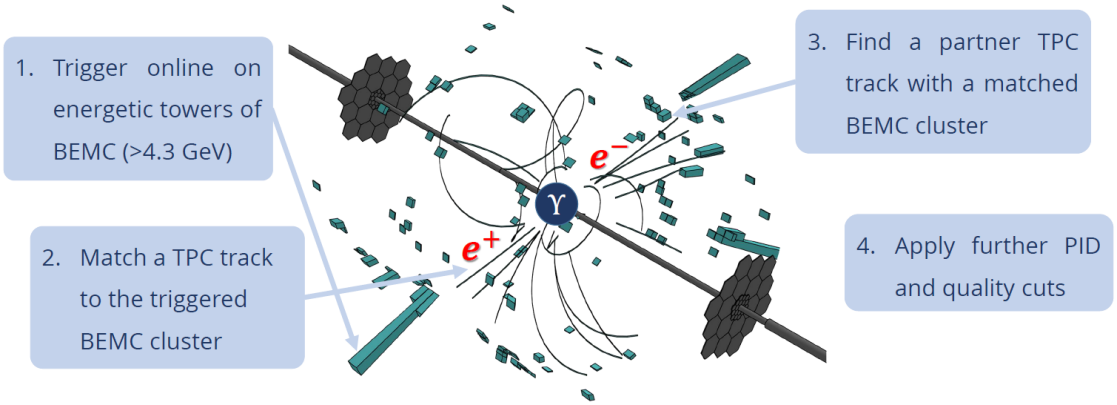

Fig. 5.3: Cartoon of the employed reconstruction algorithm. The curved black lines represent the TPC tracks and the green bars denote the BEMC towers.

5.2.1 Selection with TPC

Charged particle tracks reconstructed via TPC are subjected to the following set of cuts:

- the track is a primary track, i.e. matched to the primary vertex,
- $nHitsFit \geq 25$; hit-points in TPC used for the track fitting,
- $nHitsdEdx \geq 10$; hit-points in TPC used for the $\mathrm{d}E/\mathrm{d}x$ determination,
- $nHitsRatio \geq 0.52$; ratio of the hit-points used in a given TPC sector and the possible maximum of the track,
- DCA< 0.75 cm; distance of the closest approach to the primary vertex,
- $-1.5 < n\sigma_e < 3$; number of Gaussian deviations from the predicted $\langle \mathrm{d}E/\mathrm{d}x \rangle$ value for electrons,
- $|\eta| < 1.0$,
- $p > 3.5$ GeV/c,
- $p > 4.5$ GeV/c for at least one daughter,
- $|y| < 0.5$ for a daughter pair,
- $p_\mathrm{T} < 10$ GeV/c for a daughter pair.

Distribution of the $n\sigma_e$ with the applied cut is shown in Fig. 5.4. The kinematics variables—η, φ, and p—are plotted in Fig. 5.5. The peak at zero corresponds to the tracks that are not primary. Finally, the daughter pair kinematics—p_T and y—can be found in Fig 5.6.

5.2.2 Selection with BEMC

Apart from the triggering, the BEMC is also utilised to help identify electrons. PID traits of the calorimeter are not based on single towers but on clusters of three neighbouring towers

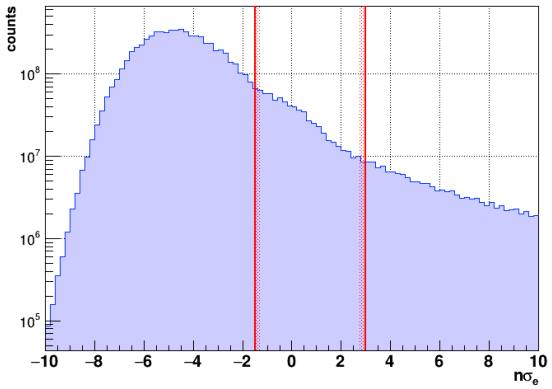

Fig. 5.4: *THIS ANALYSIS*: Distribution of the $n\sigma_e$ of all tracks. Red lines represent the applied cuts.

with the highest energy deposit. A TPC track successfully matched to such cluster needs to subsequently fulfil following conditions:

- $0.75 < E/p < 1.5$; deposited energy in a cluster divided by the track momentum,
- $R = \sqrt{\Delta\eta^2 + \Delta\varphi^2} < 0.025$; distance between the cluster *centre of gravity* and the projection of the track to the BEMC.

The BEMC-related distributions and cuts can be found in Fig. 5.7.

5.3 Raw yield reconstruction

The Υ raw yield is reconstructed from the distribution of the invariant mass of an electron-positron pair, which can be calculated as follows,

$$m^2_{e^+e^-} = (E_{(1)} + E_{(2)})^2 - (\vec{p}_{(1)} + \vec{p}_{(2)})^2 \ , \tag{5.1}$$

5.3.1 Combinatorial background

Due to the fact that electrons in an event can come from many sources other than the Υ (such as γ conversions, semi-leptonic decays, other resonances), the invariant mass spectrum

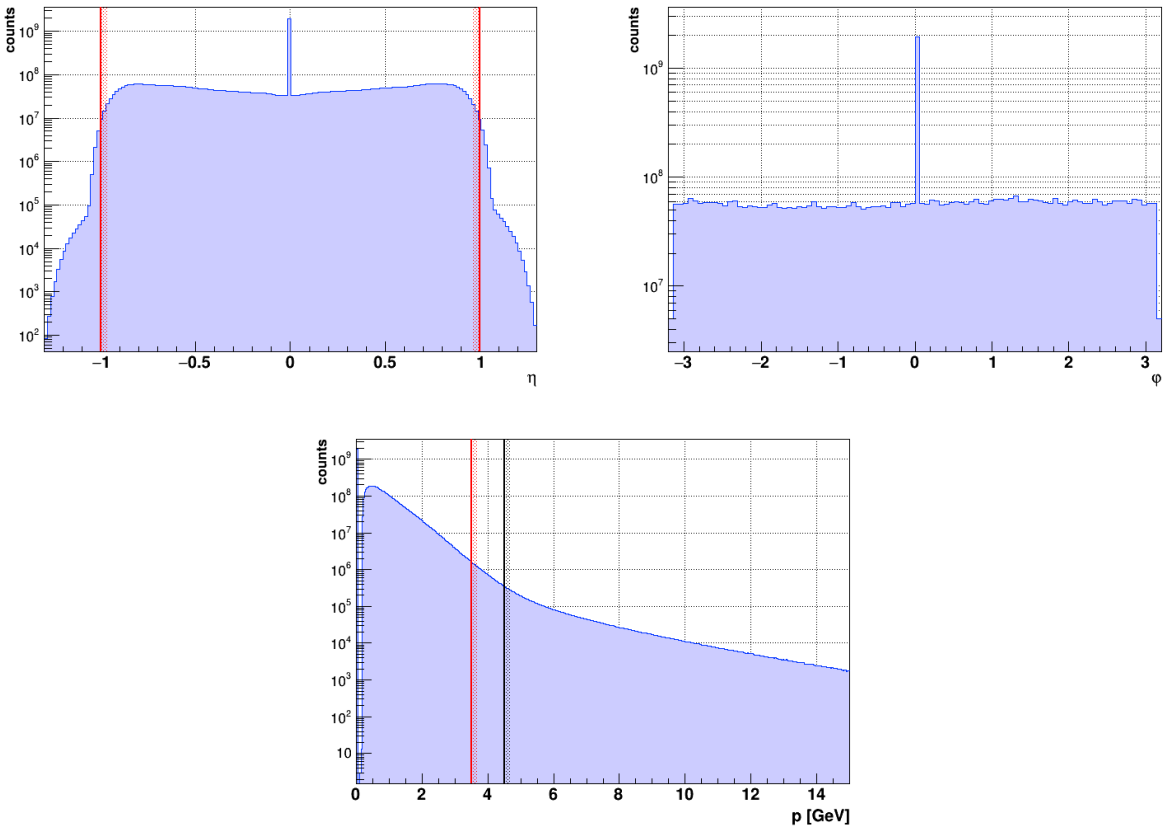

Fig. 5.5: *THIS ANALYSIS*: Distributions of the pseudorapidity η (*left*); azimuthal angle φ (*right*); and the momentum p (*bottom*). The peak at η,$\varphi = 0$ corresponds to the non-primary tracks. The red lines denote the applied cuts for all candidates, the black line represents the cut for at least one of the daughters in a pair.

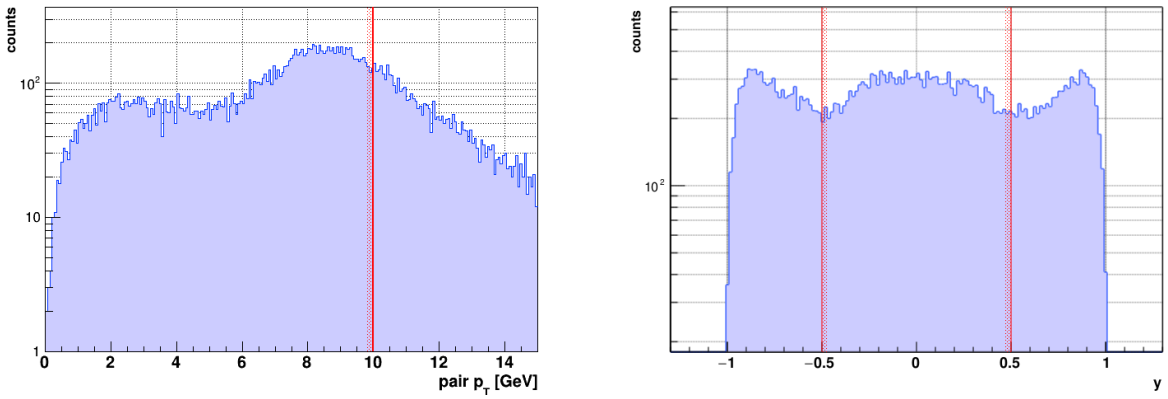

Fig. 5.6: *THIS ANALYSIS*: Distribution of the kinematics variables of the daughter pair—pair transverse momentum p_{T} (*left*) and pair rapidity y (*right*). The red lines represent the chosen selection cuts.

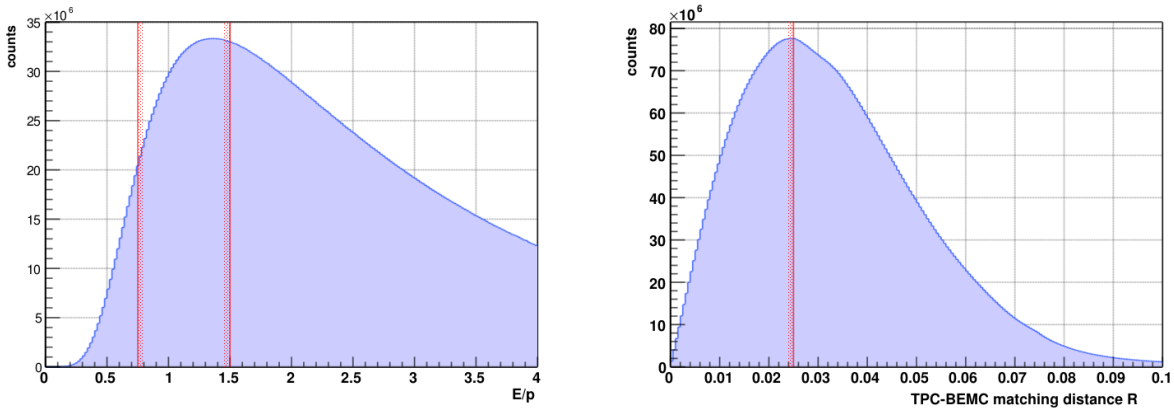

Fig. 5.7: *THIS ANALYSIS*: Distributions of the energy over momentum E/p (*left*); TPC-BEMC matching parameter R (*right*). The red lines denote the applied cuts.

is largely contaminated by background of completely uncorrelated, random pairs. This *combinatorial background* is usually modelled by forming a mass spectrum of like-signed pairs. Such pairs cannot come from any relevant decays but would still be equally susceptible to this effect.

Let us assume there are N_s sources of di-electrons in one event, which subsequently produce N_s electrons and N_s positrons. The total number of all possible unlike-sign combinations is then N_s^2. If we subtract this from the number of actual decays, we get

$$N_{+-}^{\text{comb.}} = N_s^2 - N_s = N_s(N_s - 1) \ . \tag{5.2}$$

Let us now consider the like-sign combinations, for example $(--)$. The first electron can form $N_s - 1$ like-sign pairs, the second $N_s - 2$, and further on. This gives us the total number of

$$N_{--}^{\text{comb.}} = (N_s - 1) + (N_s - 2) + ... + (N_s - N_s) \tag{5.3}$$

$$= N_s \cdot N_s - (1 - 2 - ... - N_s) = N_s \frac{N_s - 1}{2} \ . \tag{5.4}$$

This, summed with the $(++)$, can therefore describe the combinatorial background. Sometimes, the geometrical average multiplied by two is used instead, which is an equivalent method. It, however, can work better if one wants to account for different reconstruction efficiencies of e^+ and e^-, should there be any (negligible in this analysis).

5.3.2 Event mixing

Another popular method to estimate the combinatorial background is by pairing electrons and positrons from different events, thus removing any possible correlation. It benefits from much better statistical precision, that being said, its feasibility is sometimes questioned and it is not universally applicable.

In this analysis, it was found that the event mixing fails to describe the like-sign spectrum accurately, and thus was not used. This can be seen in Fig. 5.8, which shows the comparison

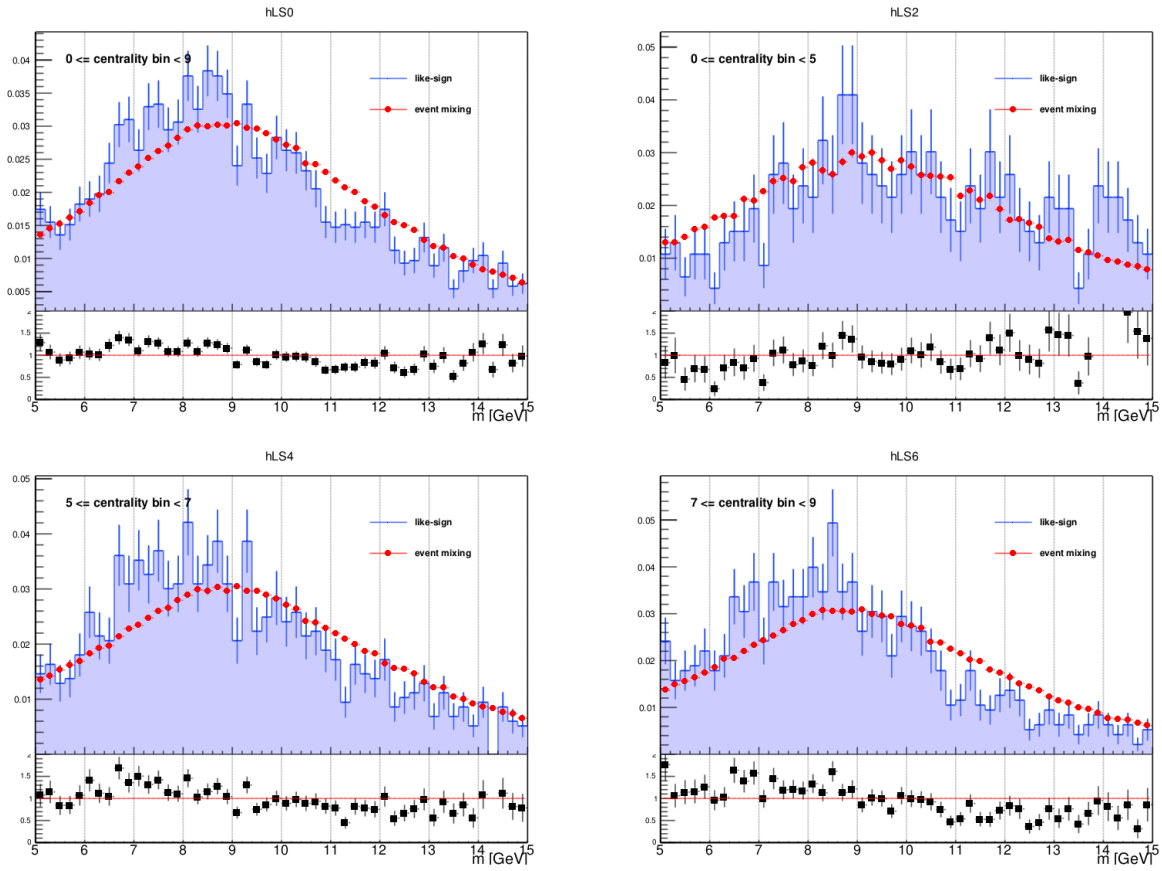

Fig. 5.8: *THIS ANALYSIS*: Comparison of the combinatorial background modelled by like-sign spectrum (blue) and event mixing (red) in different ranges of centrality, also shown with ratio plots.

of the like-sign and the event-mixed background. The electrons were paired together only from events as similar as possible (v_z, centrality), however, time-dependent irregularities in the data-taking could still be reflected in the data. This can impact the method's applicability and partially explain the seen difference.

5.3.3 Upsilon signal line-shapes

In an ideal detector and with no energy loss of the daughters, the Υ's would be represented as Breit-Wigner peaks with widths of τ^{-1}. Due to the detector momentum resolution and bremststrahlung of the electrons, the peaks take shape of the Crystal-Ball function, whose

definition is

$$f(x;\alpha,n,\bar{x},\sigma) = N \cdot \begin{cases} \exp(-\frac{(x-\bar{x})^2}{2\sigma^2}), & \text{for } \frac{x-\bar{x}}{\sigma} > -\alpha \\ A \cdot (B - \frac{x-\bar{x}}{\sigma})^{-n}, & \text{for } \frac{x-\bar{x}}{\sigma} \leqslant -\alpha \end{cases} . \tag{5.5}$$

Exact parameters of the function for each of the Υ state were determined from PYTHIA6 [46] simulation with full GEANT [47] detector response. Moreover, since this is something the analysis is rather sensitive to, the simulated line-shapes needed to be further corrected for any defects. This was done by comparing a J/ψ peak simulated in an identical fashion with the one measured[2] and incorporating additional momentum smearing to the simulation to achieve the best match between the two.

5.3.4 Correlated background

In the kinematic region of our interest, apart from the combinatorial background, there is also a significant contamination of di-electrons coming from actual physical processes. Dominantly, these are semi-leptonic decays of B mesons and Drell-Yan processes. It has been suggested that the latter is much less significant [45].

Due to the large statistical uncertainty of the measurement, the correlated background shape could not be extracted from the data across all centralities in a consistent manner. Thus, it had to be precisely parametrised from PYTHIA+GEANT simulations. The configuration options of PYTHIA are very vast—for this reason, a set of parameters STAR-HF–Tune was used. These parameters are optimised to reproduce the measurements of J/ψ, Υ, $D \to e$, and $B \to e$ spectra at the STAR experiment as accurately as possible.

For this work, we simulated only the $B\bar{B}$ decays, with a requirement for the primordial b-quarks to be created with a transverse momentum of at least 5 GeV/c. This parameter biases the invariant mass spectrum slightly to the right w.r.t. to the default zero value.

[2]The J/ψ meson is much more abundant than the Υ and for this reason suffers from significantly smaller statistical uncertainty, which makes the comparison possible and unambiguous.

Nevertheless, its effect is not too large (a shift of $\sim$ 1 GeV/c^2) since the decay electrons generally carry only a small fraction of these momenta. Moreover, the $B\bar{B}$ spectrum with this bias, is found to be very well consistent with spectra also including the Drell-Yan and incorporating a de-correlation of the b quarks in η and φ before hadronisation, which is to some extent expected in the QGP.

5.3.5 Signal extraction

Raw yields of the Υ states were extracted from the unlike-sign mass spectrum by using unbinned maximum likelihood fit. This method has been suggested to be more appropriate for low-count data [48] and was performed with the RooFit toolkit—a ROOT extension designed for data modelling. [49]

The following fitting strategy was found to be the most reliable across all centralities:

1. Fit the like-sign mass spectrum in the $(6; 14)$ GeV/c^2 range with a third-order Chebychev polynomial and fix its shape as well as magnitude,

2. build the probability distribution for the correlated background directly from the histogram from the simulation instead of using a function parametrisation to avoid unnecessary bias,

3. use the Υ line-shapes and fix the ratio of the $\Upsilon(2S)$ and the $\Upsilon(3S)$ to the world-wide average (0.689:0.311) [51],

4. fit the unlike-sign mass spectrum in the $(6; 14)$ GeV range with the composite probability distribution and extract the $\Upsilon(1S)$ and $\Upsilon(2S + 3S)$ yields,

5. evaluate the systematic uncertainties associated with the signal extraction by

    - omitting step (1) and subtracting the like-sign spectrum from the unlike-sign one in step (4),
    - varying the fit ranges to $(5.5; 14)$ and $(6; 14.5)$,

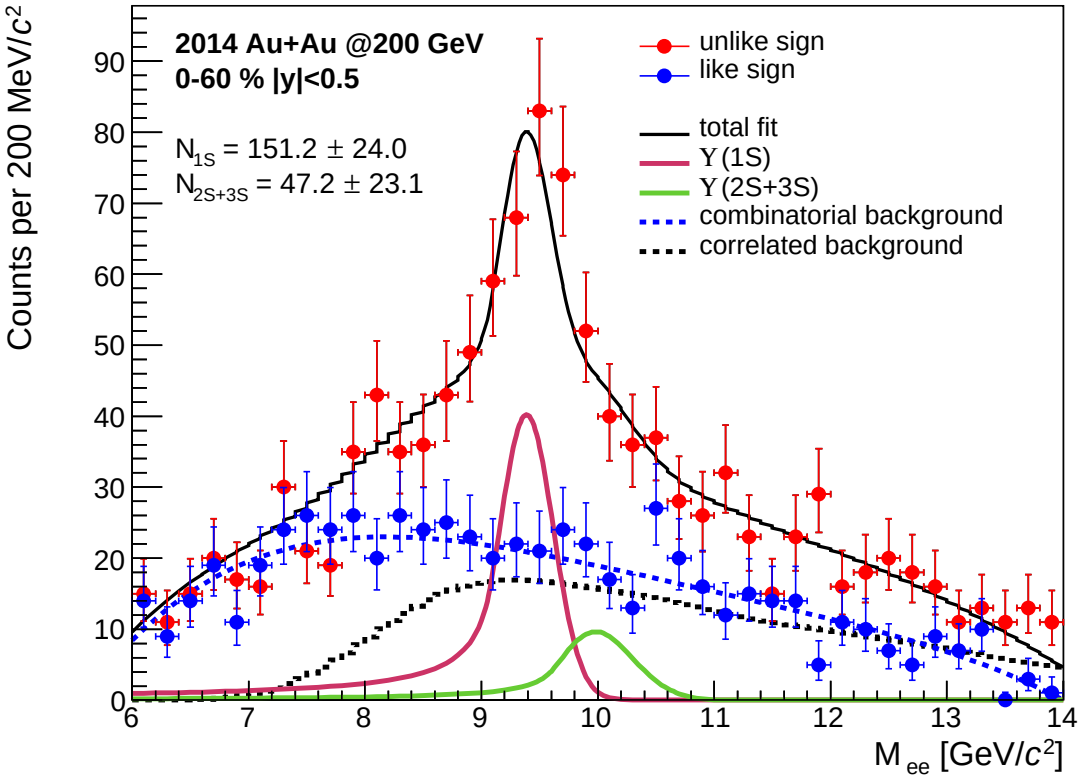

Fig. 5.9: *THIS ANALYSIS*: Reconstructed di-electron invariant mass spectrum with the composite fit of the Υ signal in the 0-60% centrality class.

- changing the widths σ of the Crystal-Ball functions by $\pm 10\%$,
- using values of 4.5 and 5.5 GeV/c for the minimum p_{T} in the correlated background simulation,
- choosing a ratio of (1:0) for the $\Upsilon(2S)$ and $\Upsilon(3S)$ states, which would correspond to a full dissociation of the latter.

The fitted invariant mass spectrum, in the 0-60% centrality class at mid-rapidity $|y| < 0.5$, is plotted in Fig. 5.9. The results for the 30-60%, 10-30%, and 0-10% centralities are shown in Fig. 5.10. A clear Υ signal is observed in all of these.

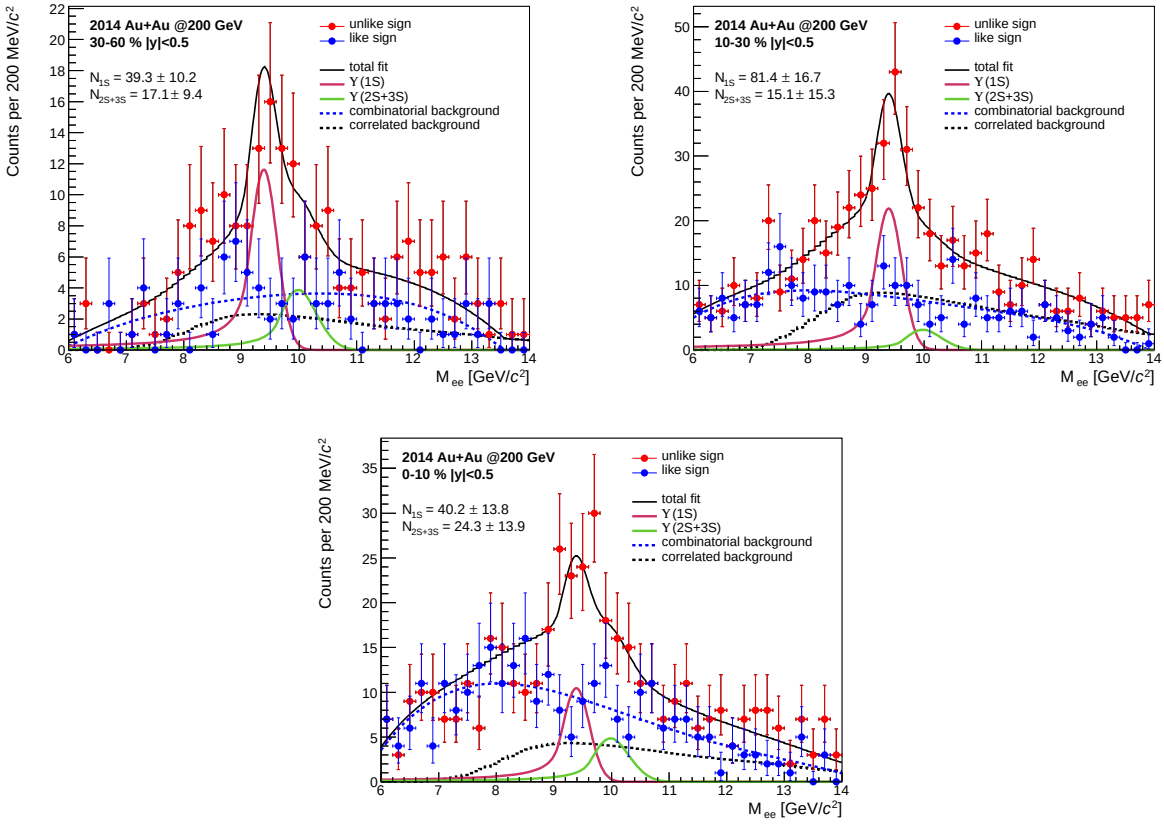

Fig. 5.10: *THIS ANALYSIS*: Reconstructed di-electron invariant mass spectrum with the composite fit of the Υ signal in the 30-60%, 10-30%, and 0-10% centrality classes.

5.4 Reconstruction efficiency and detector acceptance

Precise knowledge of the total efficiency for the Υ reconstruction is one of the most vital aspects of the measurement. To determine it, we embed a PYTHIA6-simulated Υ signal, incorporate a full detector response with GEANT, and embed it into real events[3]. Such data are subsequently analysed with the same methods as with the real data and by comparing its results with the a priori known Monte Carlo truth, efficiencies can be inferred. Some efficiencies can also be determined directly from the real data.

5.4.1 Embedding

The MC sample was generated with the following parameters:

- 900K events; 300K for each Υ state; 1 Υ per event,
- inclusion of events from both the *lowmid* and the *high* datasets,
- the Υ's are generated with a uniform distribution in $|y| < 1.2$, $\varphi < 2\pi$, and $0 < p_{\mathrm{T}} < 10$.

Henceforth, unless stated otherwise, we will show efficiencies for the $\Upsilon(1S)$ only, with no discrimination between centrality and *lowmid* and *high*, even though in the analysis we determined this individually for each state, centrality bin, and sub-dataset.

5.4.2 Daughters acceptance, trigger efficiency, tracking

Single electron TPC acceptance and trigger efficiency, as functions of the electron momentum, are plotted in Fig. 5.11. Unlike the simulation, the real online trigger threshold is based on the 4 bit–shifted value of the tower ADC, referred to as DSM. For BHT2, the DSM threshold is 19, which corresponds to the ADC of $(18 >> 4) = 306$. However, for the ADC, the trigger turn-on actually starts at ~ 297. A value of ADC ± 9, corresponding to the width of a $\mathrm{ADC}|_{\mathrm{DSM=const.}}$ simulated Gaussian, was used as the threshold variation to determine the systematics.

[3]Such simulation is referred to as *embedding*.

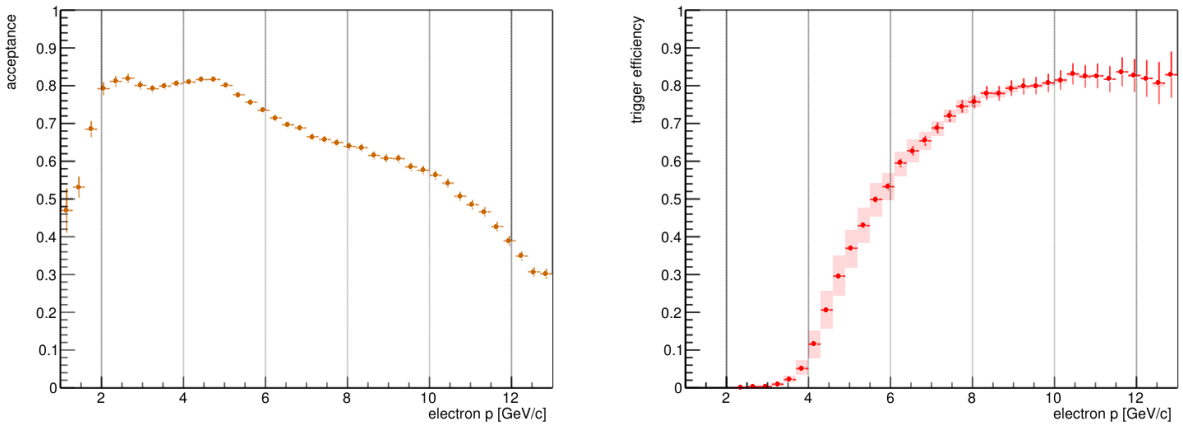

Fig. 5.11: *THIS ANALYSIS*: Single-electron TPC acceptance (*left*) and single-electron trigger efficiency of the BHT2 trigger (*right*) as functions of the electron momentum p.

Tracking efficiency and efficiency of the track quality cuts can be found in Fig. 5.12. Flat systematic uncertainty of $\sim 5\%$ was assumed for the tracking efficiency, a value adopted from other hadron analyses at STAR [52]. Conservatively, we assume a full correlation of this for the two tracks, which results in a $2 \times 5.8\%$ uncertainty for the yield.

5.4.3 BEMC-PID efficiency

Single-electron efficiencies of the E/p PID and of the BEMC-TPC matching are shown in Fig. 5.13. Systematic uncertainty of the E/p was determined by varying the cut values by 1 σ, which is the error of E/p stemming from the energy and momentum resolution and was evaluated at the cut boundaries by Monte Carlo. As for the matching, we also varied the R cuts by the mean pointing resolution of a TPC track projected to the BEMC.

5.4.4 TPC-PID efficiency

Instead of the embedding, the $n\sigma_e$ cut efficiency was determined directly from the real data. Since the $n\sigma_e$ is constructed so that at any p it gives the distance between the measured $\mathrm{d}E/\mathrm{d}x$ and the Bichsel-prediction in number of Gaussian σ's, the efficiency should be easily

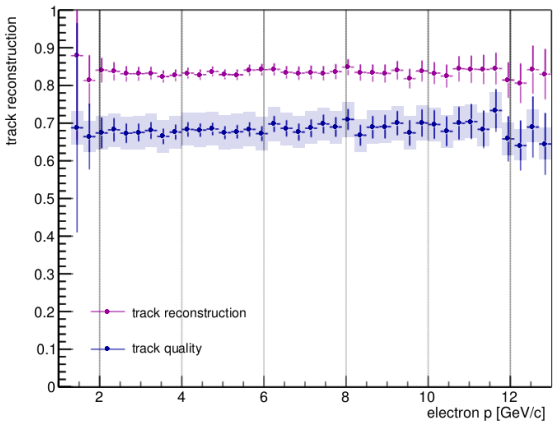

Fig. 5.12: *THIS ANALYSIS*: Single-electron tracking efficiency as a function of the electron momentum p.

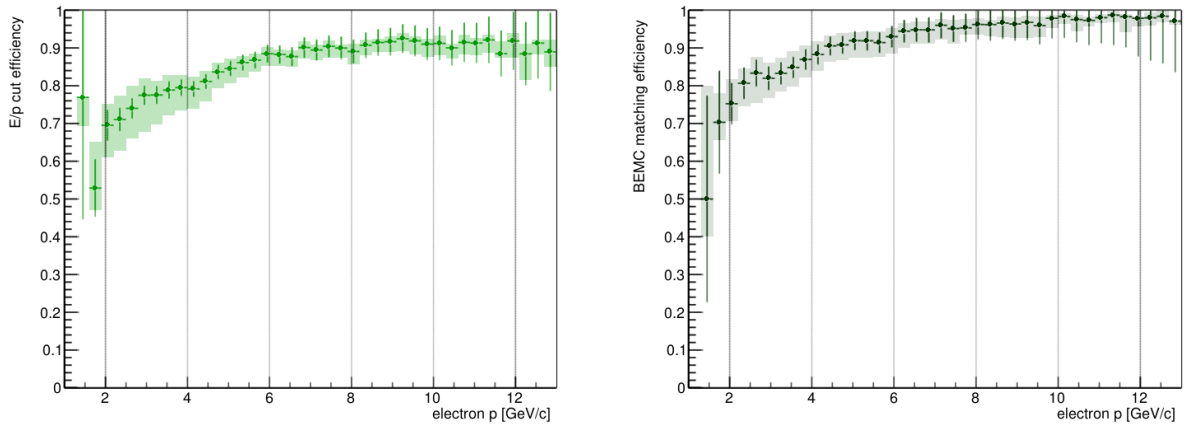

Fig. 5.13: *THIS ANALYSIS*: Single-electron efficiency of the E/p (*left*) and the TPC-matching parameter R (*right*) cuts as functions of the electron momentum p.

calculable because the $n\sigma_e$ distribution for electrons should be a Gaussian with $\mu = 0$, $\sigma = 1$. However, this is not completely true (usually $\mu \sim -0.5$, $\sigma \sim 1$) and thus the efficiency must be determined without this assumption.

Due to the large contamination by pions, the μ and σ of the electron Gaussian cannot be pinpointed accurately when selecting electrons by the standard means employed in this analysis. For this reason, a high-purity sample of electrons coming from photon conversions ($m_{ee} < 100$ MeV/c^2) was utilised. Fits of the $n\sigma_e$ distributions with three Gaussians representing electrons, pions, and kaons+protons—in different momentum bins—can be seen in Fig. 5.14. The resulting $n\sigma_e$ cut efficiency is then plotted in Fig. 5.15, along with the parametrisation and systematic uncertainty.

5.4.5 Total reconstruction efficiency

The total reconstruction efficiency incorporating everything stated above plus efficiencies of the cuts on kinematics and DCA can be found in Fig. 5.16 as a function of the Upsilon p_{T}, along with the different contributions. Due to the interplay of the shapes of the different sources, the final efficiency is almost independent on the Upsilon p_{T}. The average value of the efficiency for all Υ states in different centrality bins is plotted in Fig. 5.17.

5.5 Nuclear modification factor

The final result of this analysis is the nuclear modification factor R_{AA} as a function of the mean number of participants $\langle N_{\mathrm{part}} \rangle$. First, the invariant Υ yield is calculated as follows,

$$\frac{dN_{\Upsilon}^{\mathrm{inv.}}}{dp_{\mathrm{T}}dy} = \frac{N_{\Upsilon}^{\mathrm{raw}}}{\varepsilon_{\Upsilon} \cdot \int L\,dt \cdot \sigma_{\mathrm{Au+Au}}^{\mathrm{inel}} \cdot \Delta_{\mathrm{cent.}} \cdot \Delta y}\ , \tag{5.6}$$

where $N_{\Upsilon}^{\mathrm{raw}}$ is the raw yield of the given state extracted from the spectra, ε_{Υ} its total reconstruction efficiency and acceptance, $\int L\,dt$ the integrated luminosity of the sample, $\sigma_{\mathrm{Au+Au}}^{\mathrm{inel}} = 6$ b the total inelastic cross-section of an Au+Au collision at $\sqrt{s_{\mathrm{NN}}} = 200$ GeV [52],

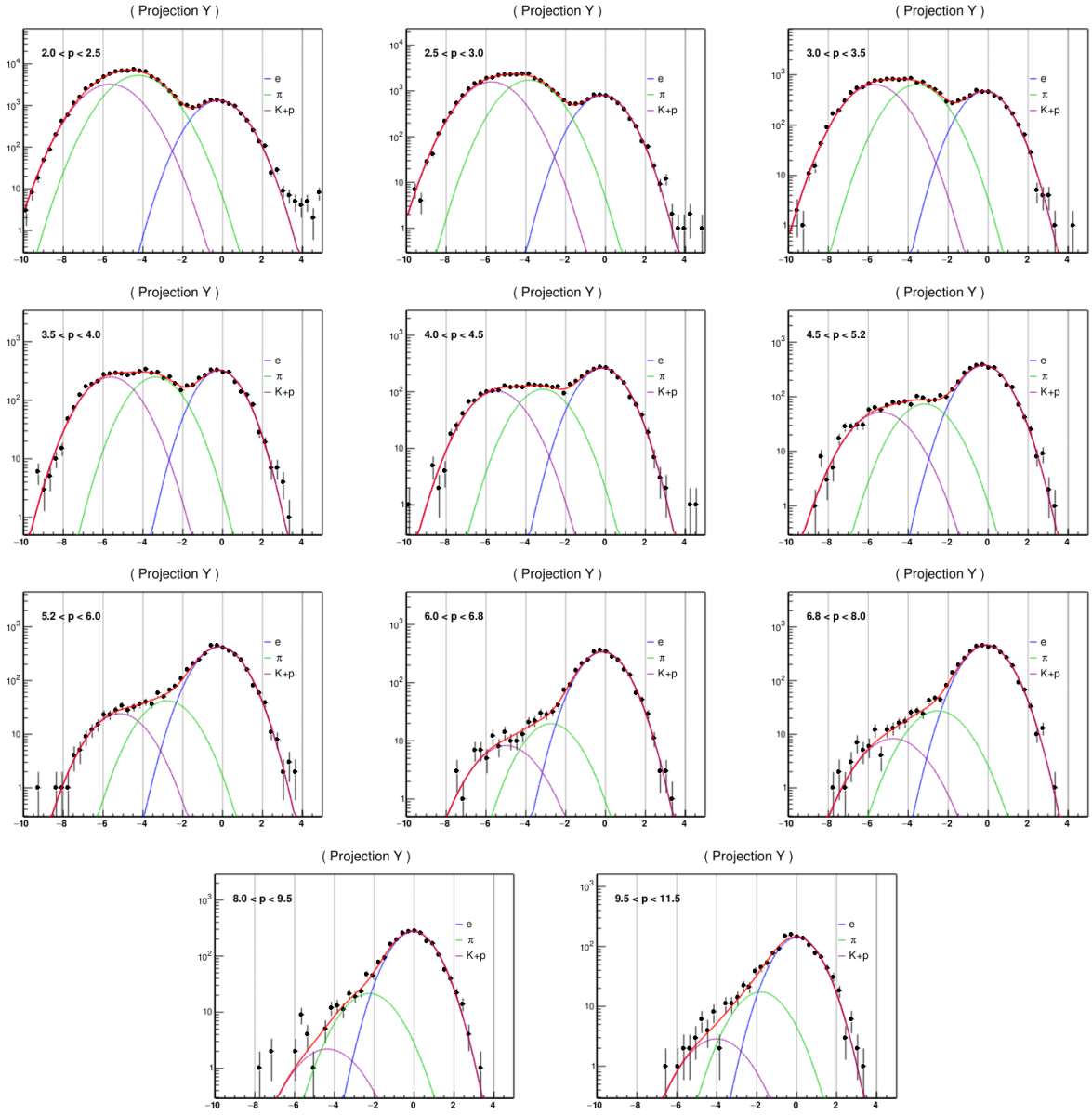

Fig. 5.14: *THIS ANALYSIS*: The $n\sigma_e$ distributions for electron candidates coming from photon conversions $m_{ee} < 100$ MeV/c^2 in different momentum bins, plotted together with three Gaussian fits corresponding to electrons, pions, and kaons and protons. The x-axis values represent the measured $n\sigma_e$.

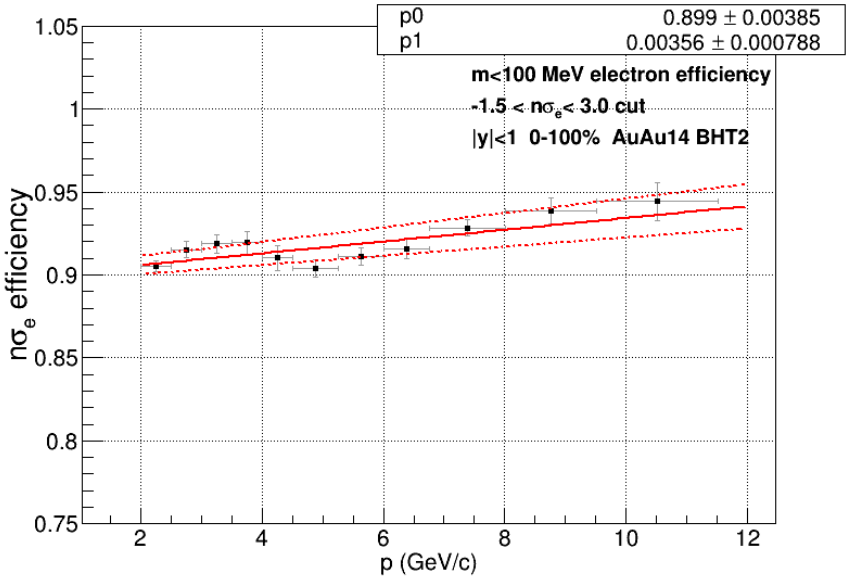

Fig. 5.15: *THIS ANALYSIS*: Single-electron efficiency of the $n\sigma_e$ cut as a function of the electron momentum p. Solid red line represents the first-order polynomial parametrisation and the dashed lines its systematic uncertainty.

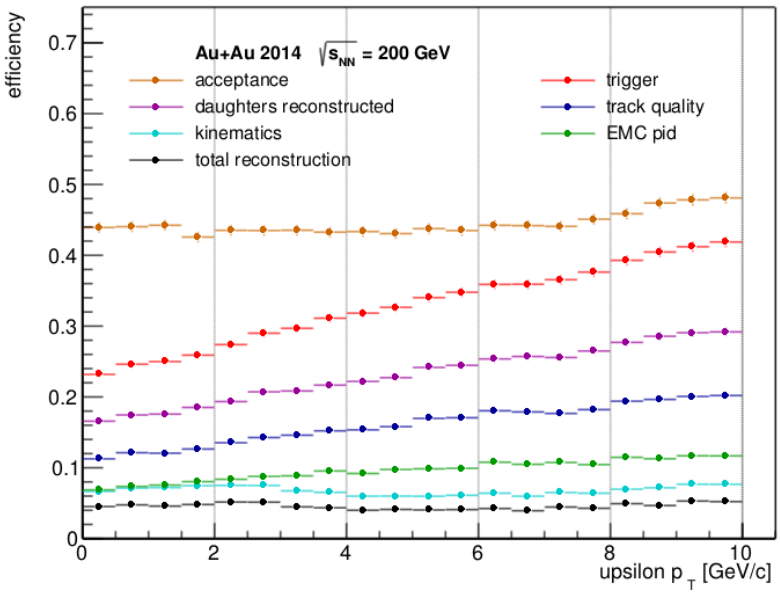

Fig. 5.16: *THIS ANALYSIS*: Reconstruction efficiency of the $\Upsilon(1S)$ as a function of its p_{T}. Effects of various components are also shown as different colour points, multiplicatively.

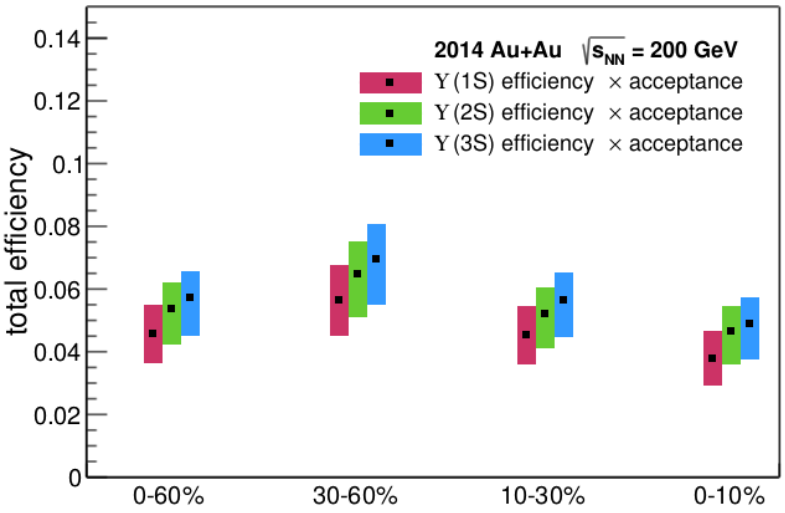

Fig. 5.17: *THIS ANALYSIS*: Values of the total reconstruction efficiency in different centrality classes for the $\Upsilon(1S)$, $\Upsilon(2S)$, and $\Upsilon(3S)$.

$\Delta_{\text{cent.}}$ the size of the centrality bin (for instance $\Delta_{\text{cent.}} = 0.3$ for the 30-60% bin), and $\Delta y = 1.0$ the size of the rapidity window. The nuclear modification factor is then determined by dividing the invariant yield with a scaled cross-section in p+p collisions $\frac{d\sigma_\Upsilon^{pp}}{dp_T dy}$ as

$$R_{AA} = \frac{\sigma_{pp}^{\text{inel}}}{\langle N_{\text{coll}} \rangle} \frac{\frac{dN_\Upsilon^{\text{inv.}}}{dp_T dy}}{\frac{d\sigma_\Upsilon^{pp}}{dp_T dy}} \ , \tag{5.7}$$

where $\sigma_{pp}^{\text{inel}} = 42$ mb is the total inelastic cross-section of a p+p collision and $\langle N_{\text{coll}} \rangle$ the mean number of binary collisions [52]. The value of $81.0 \pm 5.2\,(\text{stat.})\,^{+7.6}_{-7.7}\,(\text{syst.})$ pb was chosen as the mid-rapidity $|y| < 0.5$ p+p–reference. [50]

The nuclear modification factors of the $\Upsilon(1S)$ and the $\Upsilon(2S+3S)$ as functions of $\langle N_{\text{part.}} \rangle$ are shown in Fig. 5.18, along with the uncertainties. Sources of the systematic uncertainties and their effect on the R_{AA} are listed in Tab. 5.2.

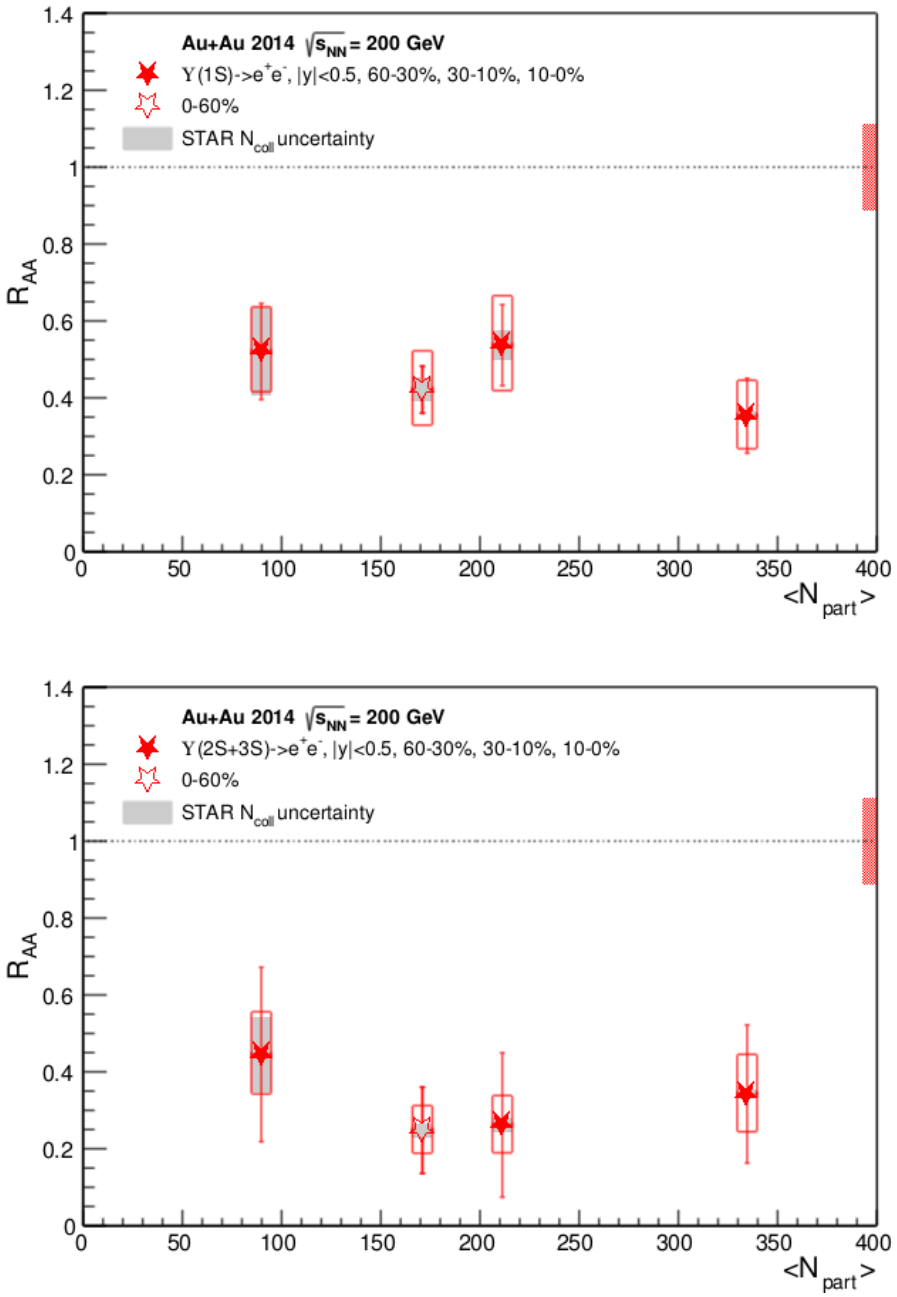

Fig. 5.18: *THIS ANALYSIS*: The nuclear modification factor of the $\Upsilon(1S)$ (*top*) and the $\Upsilon(2S+3S)$ (*bottom*) as a function of the mean number of participants $\langle N_{\text{part}} \rangle$. Statistical uncertainties are represented by the vertical lines and systematic uncertainties by the open boxes. Common uncertainty of the normalisation and the uncertainty of the $\langle N_{\text{coll}} \rangle$ determination are also shown, denoted as the full box around unity and grey boxes respectively.

Systematic uncertainty	%	Systematic uncertainty	%
tracking	$^{+15.1}_{-11.6}$	kinematics cuts	± 6.3
trigger efficiency	± 4.5	signal extraction	± 4.9
E/p	± 8.7	sampled luminosity	± 8
R	± 9.5	polarisation	± 3

Tab. 5.2: Sources of systematic uncertainties on R_{AA} for $\Upsilon(1S)$ in the 0-60% centrality class.

5.6 Discussion

The nuclear modification factors R_{AA} for the ground state and for the excited states—measured in the di-electron channel in dataset from Run 14—are found to be

$$\Upsilon(1S) \;\to\; R_{AA}|^{0-60\%}_{|y|<0.5} = 0.42 \pm 0.06\,(\text{stat.}) \pm 0.10\,(\text{syst.})\;, \tag{5.8}$$

$$\Upsilon(2S+3S) \;\to\; R_{AA}|^{0-60\%}_{|y|<0.5} = 0.25 \pm 0.11\,(\text{stat.}) \pm 0.06\,(\text{syst.})\;. \tag{5.9}$$

These results suggest that the excited states $\Upsilon(2S)$ and $\Upsilon(3S)$ seem to be generally more suppressed in Au+Au collisions at $\sqrt{s_{\text{NN}}} = 200$ GeV than the ground state $\Upsilon(1S)$, although the results suffer from large uncertainties. This result is consistent with the expectations coming from the phenomenon of sequential melting, see Chapter 3.

In order to increase the precision, let us combine our results with other latest measurements at STAR. The updated R_{AA}'s can be seen in Fig. 5.19. Using these, we can now see signs of a trend—with increased centrality, the suppression for all states increases as well. In the most central collisions, there is now

$$\Upsilon(1S) \;\to\; R_{AA}|^{0-10\%}_{|y|<0.5} = 0.46 \pm 0.05\,(\text{stat.}) \pm 0.04\,(\text{syst.})\;, \tag{5.10}$$

$$\Upsilon(2S+3S) \;\to\; R_{AA}|^{0-10\%}_{|y|<0.5} = 0.21 \pm 0.08\,(\text{stat.}) \pm 0.05\,(\text{syst.})\;. \tag{5.11}$$

Conclusions about direct suppression of the $\Upsilon(1S)$ at RHIC cannot be made, because even in the most central collisions, the measured R_{AA} can be explained by absence of feed-down due to total suppression of the excited states.

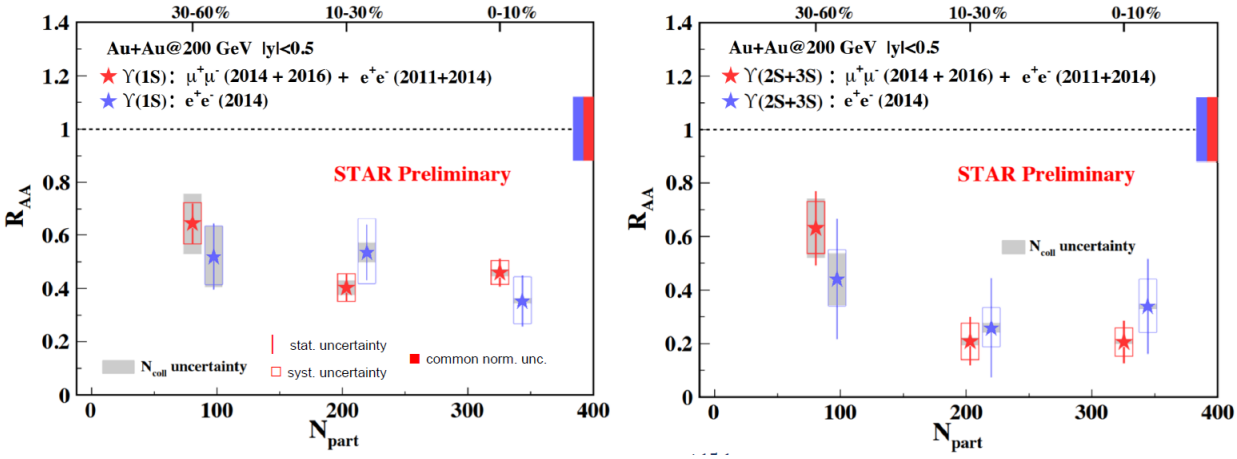

Fig. 5.19: *THIS ANALYSIS*: The nuclear modification factor of the $\Upsilon(1S)$ (*left*) and the $\Upsilon(2S+3S)$ (*right*) as a function of the mean number of participants $\langle N_{\text{part}} \rangle$. Blue points represent this analysis's contribution towards the combined results (red points). Statistical uncertainties are represented by the vertical lines and systematic uncertainties by the open boxes. Common uncertainty of the normalisation and the uncertainty of the $\langle N_{\text{coll}} \rangle$ determination are also shown, denoted as the full box around unity and grey boxes respectively.

In peripheral collisions, the $\Upsilon(1S)$ and $\Upsilon(2S+3S)$ seem to be similarily suppressed—this is consistent with the idea that the QGP was not created as the energy density was not sufficiently high. There, the measured suppression can be attributed mostly to the CNM effects, which are not expected to discriminate between the Υ states at RHIC energies.

Summary

Principal objective of this thesis is to introduce the author's measurements of Υ production in Au+Au collisions at $\sqrt{s_{\mathrm{NN}}} = 200$ GeV. Heavy quarkonia are important probes of the quark-gluon plasma, namely for their possible dissociation in the deconfining medium, which occurs for different quarkonium states at different temperatures. Basic concepts and findings about heavy-ion collisions, the QGP, and CNM effects are also overviewed.

In the analysis, the di-electron invariant mass spectrum with a clear Υ(1S) and Υ(2S+3S) signal was reconstructed in data from 2014. Furthermore, the Υ signals were carefully extracted. Expected signal shapes and contributions from correlated background sources were obtained via Monte Carlo simulations. The like-sign method was employed to estimate the combinatorial background, although event-mixing was also considered.

The measured raw yields were corrected for reconstruction efficiencies, which were determined by a combination of embedding Υ signal from simulations including full detector response into real events and a high-purity electron-enhanced data sample from photon conversions. From this, the nuclear modification factor was obtained and reported as a function of mean number of participants for both the ground and the excited states.

The $\Upsilon(2S + 3S)$ appear to be generally more suppressed than $\Upsilon(1S)$, even more so in central collisions, which becomes clearer after combining this analysis' results with other Υ measurements at STAR. This observation is consistent with the phenomenon of sequential melting—at RHIC energies, the temperature is sufficiently high for the excited states to be largely suppressed. Greater precision and better understanding of feed-down is necessary in order to draw any conclusion on the direct ground-state suppression.

Bibliography

[1] ABELEV, B., et al. (ALICE Collaboration). Centrality determination of Pb-Pb collisions at $\sqrt{s_{\mathrm{NN}}}$=2.76 TeV with ALICE. *Physical Review C*. Vol. 88 (2013).

[2] MILLER, L., et al. Glauber Modeling in High Energy Nuclear Collisions. *Annual Review of Nuclear and Particle Science*. Vol. 57 (2007).

[3] SARKAR, S., et al. *The Physics of the Quark-Gluon Plasma A: Introductory Lectures.* Springer, c2010. ISBN 978-3-642-02286-9.

[4] *Studying the Phase Diagram of QCD Matter at RHIC* [online]. STAR Collaboration. [ac. 1/05/18]. Available at: http://drupal.star.bnl.gov/STAR/system/files/BES_WPII_ver6.9_Cover.pdf .

[5] CHODOS, A., et al. New extended model of hadrons. *Physical Letters D*. Vol. 9.

[6] WONG, C. *Introduction to High-Energy Heavy Ion collisions*. Utopia Press, 1st edition, c1994. ISBN 978-981-02-0263-7.

[7] BAZAVOV, A., et al. Equation of state in $(2+1)$-flavor QCD. *Physical Letters D*. Vol. 90 (2014).

[8] TAWFIK, A., et al. Balance Function in High-Energy Collisions. *Advances in High Energy Physics*. Vol. 2015 (2015).

[9] *Research* [online]. Relativistic Heavy Ion Physics Group, Rice University. [ac. 1/05/18]. Available at: http://wl33.web.rice.edu/research.html .

[10] ABELEV, B., et al. (ALICE). Elliptic flow of charged particles in Pb-Pb collisions at 2.76 TeV. *Physical Review Letters*. Vol. 105 (2010).

[11] ABELEV, B., et al. (ALICE). Elliptic flow of identified hadrons in Pb-Pb collisions at $\sqrt{s_{\mathrm{NN}}} = 2.76$ TeV. *Journal of High Energy Physics*. Vol. 2015 (2015).

[12] KIM, E. System and rapidity dependence of baryon to meson ratios at RHIC. *Nuclear Physics A*. Vol. 774 (2006).

[13] *Quantum Chromodynamics* [online]. Atominstitut, TU Wien. [ac. 1/05/18]. Available at: https://ati.tuwien.ac.at/research_areas/nuclear_and_particle_physics/research/fundamental_interactions/quantum_chromodynamics/EN/ .

[14] *Recent QGP studies at LHC/RHIC and future plans* [online]. Shin Esumi [ac. 1/05/18]. Available at: http://silver.j-parc.jp/hadron/hadron_seminar/150513SEsumi.pdf .

[15] D'ENTERRIA, D. Quark-gluon matter. *Journal of Physics G*. Vol. 34 (2007).

[16] MANUEL, C. The Stopping Power of Hot Nuclear Matter. *American Physical Society*. Vol. 7 (2014).

[17] FACCIOLI, P., et al. Study of psi and chic decays as feed-down sources of J/psi hadroproduction. *Journal of High Energy Physics*. Vol. 10 (2008).

[18] EMERICK, A., et al. Bottomonia in the Quark-Gluon Plasma and their Production at RHIC and LHC. *European Physics Journal A*. Vol. 48 (2012).

[19] VOGT, R. *Ultrarelativistic Heavy-Ion Collisions.* Elsevier, 1st edition, c2007. ISBN 9780444521965.

[20] EIDELMAN, S., et al. (Particle Data Group). Review of Particle Physics. *Physical Letters B*. Vol. 592.

[21] SATZ, H. Colour screening in SU(N) gauge theory at finite temperature. *Nuclear Physics A*. Vol. 418 (1984).

[22] MATSUI, T., SATZ., H. J/ψ Suppression by Quark-Gluon Plasma Formation. *Physical Letters B*. Vol. 178.

[23] FERBEL, T. *Techniques and Concepts of High Energy Physics X.* Springer Netherlands, 1st edition, c1999. ISBN 9789401146890.

[24] ADYLOV, G.T. The pion radius. *Physical Letters B*. Vol. 51 (1974).

[25] ARNALDI, R. J/psi production in p-A and A-A collisions at fixed target experiments. *Nuclear Physics A*. Vol. 830 (2009).

[26] MOCSY, A. Potential Models for Quarkonia. *European Physical Journal C*. Vol. 61 (2009).

[27] SATZ, H. Probing the states of matter in QCD. *Journal in Modern Physics A*. Vol. 28 (2013).

[28] *CMS observes melting of Upsilon particles in heavy-ion collisions* [online]. CMS Collaboration [ac. 1/05/18]. Available at: http://cms.web.cern.ch/news/cms-observes-melting-upsilon-particles-heavy-ion-collisions .

[29] ABELEV, B., et al. (ALICE) J/psi suppression at forward rapidity in Pb-Pb collisions at $\sqrt{s_{\mathrm{NN}}} = 2.76$ TeV. *Physical Review Letters*. Vol. 109 (2012).

[30] SATZ, H., et al. An Introduction to the Spectral Analysis of the QGP. *Lecture Notes in Physics* . Vol. 785 (2010).

[31] ABELEV, B., et al. (ALICE) Measurement of charm production at central rapidity in proton-proton collisions at $\sqrt{s_{\mathrm{NN}}} = 2.76$ TeV. *Journal of High Energy Physics*. Vol. 07 (2012).

[32] ABELEV, B., et al. (ALICE) J/psi elliptic flow in Pb-Pb collisions at $\sqrt{s_{\mathrm{NN}}} = 5.02$ TeV. *Physical Review Letters*. Vol. 119 (2017).

[33] HUANG, X. Measurement of J/psi production in Au+Au collisions at $\sqrt{s_{\mathrm{NN}}} = 200$ GeV by the STAR experiment. *Nuclear and Particle Physics Proceedings*. Vol. 289-290 (2017).

[34] VOGT, R. Shadowing Effects on J/psi and Y Production at the LHC. *Physical Reviews C*. Vol. 92 (2015).

[35] CRONIN, J.W., et al. Production of hadrons at large transverse momentum at 200, 300, and 400 GeV. *Physical Reviews D*. Vol. 11 (1975).

[36] ABELEV, B., et al. (ALICE) J/psi production and nuclear effects in p-Pb collisions at $\sqrt{s_{\mathrm{NN}}} = 5.02$ TeV. *Journal of High Energy Physics*. Vol. 73 (2014).

[37] SCOMPARIN, E. J/psi production in p-A collisions at 158 and 400 GeV: recent results from the NA60 experiment. *Nuclear Physics A*. Vol. 830 (2009).

[38] FERREIRO, E. Excited charmonium suppression in proton-nucleus collisions as a consequence of comovers. *Physical Letters B*. Vol. 749 (2015).

[39] ABELEV, B., et al. (ALICE) Suppression of psi(2S) production in p-Pb collisions at $\sqrt{s_{\mathrm{NN}}} = 5.02$ TeV. *Journal of High Energy Physics*. Vol. 12 (2014).

[40] ANDERSON, M., et al. The Relativistic Heavy Ion Collider Project: RHIC and its Detectors. *Nuclear Instruments and Methods in Physics Research A*. Vol. 499 (2003).

[41] *Relativistic Heavy Ion Collider* [online]. Brookhaven National Laboratory. [ac. 01/09/17]. Available at: https://drupal.star.bnl.gov/STAR/public/img/SketchUpSTAR .

[42] ANDERSON, M., et al. The STAR Time Projection Chamber: A Unique Tool for Studying High Multiplicity Events at RHIC. *Nuclear Instruments and Methods in Physics Research A*. Vol. 499 (2003).

[43] BEDDO, M., et al. The STAR Barrel Electromagnetic Calorimeter. *Nuclear Instruments and Methods in Physics Research A*. Vol. 499 (2003).

[44] ROOT. [software] Data Analysis Framework. [opensource]. [ac. 01/05/18]. Available at http://root.cern.ch .

[45] GAVIN, S., et al. Lepton production from charm decay in nuclear collisions at s=200 GeV and 5.5 TeV per nucleon. *Physical Review C*. Vol. 54 (1996).

[46] SJOSTRAND, T., et al. A Brief Introduction to Pythia 8.1. *Computing Physics Community*. Vol. 178 (2008).

[47] AGOSTINELLI, S., et al. GEANT4 a simulation toolkit. *Nuclear Instruments and Methods in Physics A*. Vol. 506 (2002).

[48] ARZNER, K., et al. Unbinned maximum-likelihood estimators for low-count data: Applications to faint X-ray spectra in the Taurus Molecular Cloud. *Astronomy and Astrophysics*. Vol. 468 (2007).

[49] VERKERKE, W., KIRKBY, D. The RooFit toolkit for data modeling. *Electronic Conference Proceedings Archive*. Vol. C0303241 (2002).

[50] MATONOHA, O. Measurements of the Υ meson production in Au+Au collisions at the STAR experiment *Proceedings of Science*. Vol. EPS-HEP2017 (2017).

[51] ZHA, W., et al. Systematic study of the experimental measurements on ratios of different Y states. *Physical Reviews C*. Vol. 88 (2013).

[52] ADAMCZYK, L., et al. (STAR) Suppression of Y production in d+Au and Au+Au collisions at $\sqrt{s_{\mathrm{NN}}} = 200$ GeV. *Physics Letters B*. Vol. 735 (2014).

[53] LIN, Z., KO, C. Υ absorption in hadronic matter. *Physical Letters B*. Vol. 503 (2001).

A Published papers and posters related to this work

1. Quark Matter 2018 in Venice, Italy; Poster: *"Measurements of the* Υ *meson production in Au+Au collisions at* $\sqrt{s_{NN}} = 200$ *GeV by the STAR experiment"*

2. EPS-HEP 2017 in Venice, Italy; Talk + Proceedings: *"Measurements of the* Υ *meson production in Au+Au collisions at the STAR experiment"*

PROCEEDINGS OF SCIENCE

Measurements of the Υ meson production in Au+Au collisions at the STAR experiment

Oliver Matonoha* **for the STAR collaboration**
Department of Physics
Faculty of Nuclear Sciences and Physical Engineering
Czech Technical University in Prague
Brehova 7, 115 19 Prague, Czech Republic
E-mail: oliver.matonoha@fjfi.cvut.cz

In ultra-relativistic heavy-ion collisions, creation of a novel state of matter, consisting of deconfined quarks and gluons, has been observed. Quarkonium suppression in the medium due to the colour screening effect has been viewed as a direct evidence of the formation of such matter. Moreover, different quarkonium states are expected to dissociate at different temperatures, which can be used to constrain the medium temperature. At RHIC energies, other effects, such as regeneration and co-mover absorption, are expected to be very small for the bottomonium family, which makes it a cleaner probe compared to the J/ψ meson. The nuclear modification factors for the Υ states measured in Au+Au collisions at $\sqrt{s_{\mathrm{NN}}} = 200$ GeV via both the di-muon and di-electron channels by the STAR experiment at RHIC are reported and compared with similar measurements at the LHC as well as theoretical calculations. Moreover, measurements of the Υ production in p+p and p+Au collisions are presented as well, providing a p+p reference with significantly improved precision and a quantification of the cold nuclear matter effects, respectively.

EPS-HEP 2017, European Physical Society conference on High Energy Physics
5-12 July 2017
Venice, Italy

*Speaker.

1. Introduction

Lattice QCD calculations predict that under extreme conditions, hadronic matter undergoes a phase transition and forms a new state of matter consisting of deconfined quarks and gluons, the so-called Quark Gluon Plasma (QGP). This form of matter is hypothesised to comprise the Universe in its earliest stages. Such conditions are believed to be achievable in ultra-relativistic heavy-ion collisions at the Relativistic Heavy Ion Collider (RHIC) and the Large Hadron Collider (LHC). Due to its short lifetime ($\sim$fm/c), the properties of the QGP are experimentally very challenging to measure.

One of the key probes to the QGP properties is the measurement of suppression for heavy quarkonia, e.g. J/ψ or Υ. The $c\bar{c}$ or $b\bar{b}$ pairs, due to their large masses, are created primarily before the QGP formation and their production cross-sections can be well calculated based on perturbative QCD. In the presence of the QGP, a quarkonium is expected to dissociate by the *colour screening* effect when its radius exceeds the Debye radius $r_{\mathrm{Debye}} \propto 1/T$ [1]. This dissociation is dependent on the quarkonium binding energy, and thus is expected to occur for different states at different temperatures. Thanks to this *sequential melting*, quarkonia can serve as a "QGP thermometer" [2].

Other phenomena can also influence the quarkonium production in heavy-ion collisions, such as the *statistical recombination* by coalescence of deconfined quarks at the QGP phase boundary and the *cold nuclear matter (CNM)* effects, like the inelastic interactions with co-moving hadrons. The CNM effects can be investigated in p+A collisions. Compared to J/ψ, the Υ mesons are believed to be a cleaner probe of the colour screening effect at RHIC energies, due to less susceptibility to the co-mover absorption [3] and virtually no production by recombination thanks to the b and $\bar{b}$ scarcity in the medium [4].

2. Υ reconstruction with the STAR experiment

At the Solenoidal Tracker At RHIC experiment (STAR), Υ's are reconstructed via both the di-electron and di-muon decay channels at mid-rapidity. The Time Projection Chamber (TPC) serves as the primary tracking sub-detector with full coverage in azimuth $0 < \varphi < 2\pi$ within pseudorapidity $|\eta| < 1$. It also provides particle identification (PID) via measurement of the energy loss $\mathrm{d}E/\mathrm{d}x$. For the di-electron channel, the Barrel Electromagnetic Calorimeter (BEMC) is employed. It has the same φ and η coverage as the TPC. Apart from providing electron PID via the E/p, it is also used for triggering on high-p_{T} electrons from Υ decays. Since 2013, STAR can also measure quarkonium production through the di-muon channel thanks to the instalment of the Muon Telescope Detector (MTD) placed behind the solenoidal magnet. It covers approximately 45% in azimuth within $|\eta| < 0.5$ and can be used for both identifying and triggering on muons. Whenever possible, results obtained from both of the channels are combined to enhance the statistical precision of the measurement.

3. Results

In all figures presented in this section, statistical uncertainties are shown as vertical bars and systematic ones as open boxes around the data points. Full boxes around unity denote the global uncertainties.

3.1 Υ production in p+p and p+Au collisions

Production of Υ(1S+2S+3S) has been measured via the di-electron channel in p+p collisions at $\sqrt{s} = 200$ GeV using BEMC-triggered data with an integrated luminosity of 97 pb^{-1} from 2015. Within $|y| < 0.5$, the p_{T}-integrated cross-section is measured to be $B \cdot \mathrm{d}\sigma/\mathrm{d}y = 81 \pm 5(\mathrm{stat.}) \pm 8(\mathrm{syst.})$ pb, where B is the branching ratio. As shown in the left panel of Fig. 1, the new result is consistent with the previously published result by STAR [5], but the precision is improved by a factor of 2. The new result is also in a good agreement with the trend of world-wide experimental data as well as the NLO CEM prediction [6].

In order to study the CNM effects, Υ measurements have also been carried out in p+Au collisions at $\sqrt{s_{\mathrm{NN}}} = 200$ GeV through the di-electron channel using BEMC-triggered data with an integrated luminosity of 300 nb^{-1} from 2015. The measured nuclear modification factor R_{pAu} within $|y| < 0.5$ is $0.82 \pm 0.10(\mathrm{stat.})^{-0.07}_{+0.08}(\mathrm{syst.}) \pm 0.10(\mathrm{norm.})$. The R_{pAu} is shown in the right panel of Fig. 1 as a function of rapidity. These results are consistent with previous STAR measurements in d+Au collisions [5] but have two times smaller relative uncertainties.

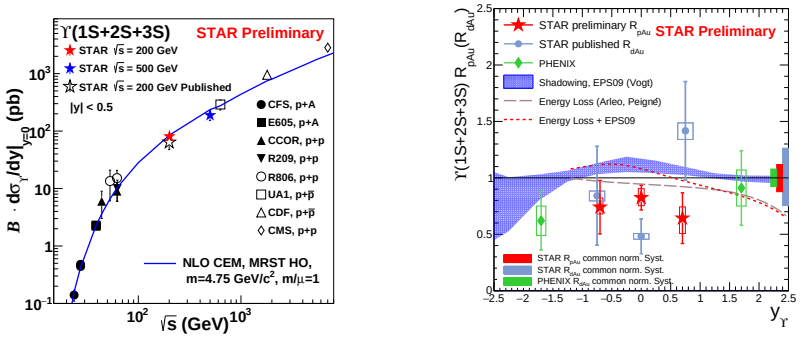

Figure 1: (*left*) Υ(1S+2S+3S) production cross-section at mid-rapidity from p+p collisions of $\sqrt{s} = 200$ GeV (red star) compared with global results and NLO CEM calculations [6]; (*right*) Υ(1S+2S+3S) nuclear modification factor R_{pAu} from p+Au collisions of $\sqrt{s_{\mathrm{NN}}} = 200$ GeV (red stars) as a function of rapidity.

3.2 Υ production in Au+Au collisions

In Au+Au collisions at $\sqrt{s_{\mathrm{NN}}} = 200$ GeV, the Υ production has been measured both in the di-electron channel (BEMC-triggered data of 1.1 nb^{-1} from 2011) and the di-muon channel (MTD-triggered data of 14 nb^{-1} from 2014). Nuclear modification factors measured in both channels are found to be consistent with each other within uncertainties, and thus are combined to further increase the precision.

The combined R_{AA} is presented in Fig. 2 as a function of the mean number of participants N_{part} in each centrality bin for both Υ(1S) and Υ(2S+3S). The excited states are more suppressed in central collisions than the ground state. Shown are also results measured by CMS in Pb+Pb collisions at $\sqrt{s_{\mathrm{NN}}} = 2.76$ TeV [7]. Whereas the Υ(1S) results are consistent, the Υ(2S+3S) appears to be less suppressed at RHIC than at the LHC. The R_{AA} extracted from the di-muon channel is also shown in Fig. 3 as a function of p_{T}. In comparison with the CMS results [7], the Υ(1S) R_{AA} is again in agreement, whilst the Υ(2S+3S) R_{AA} seems to be larger at high-p_{T} at the RHIC.

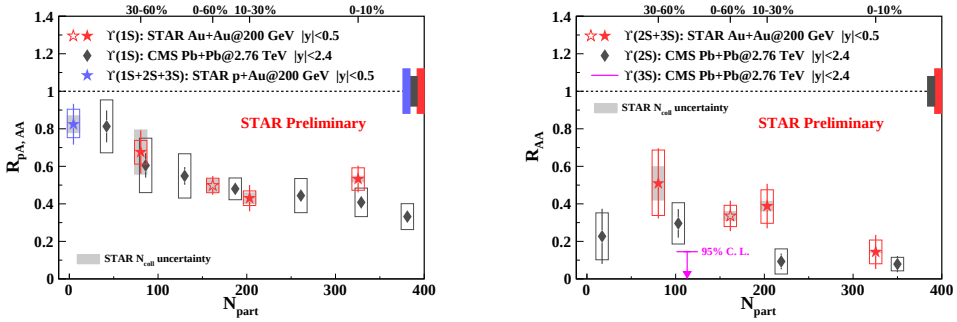

Figure 2: R_{AA} for the Υ(1S) (*left*) and the Υ(2S+3S) (*right*) at mid-rapidity as a function of N_{part} in Au+Au collisions at $\sqrt{s_{\mathrm{NN}}} = 200$ GeV (red stars). Also portrayed are the centrality integrated result (open red star), the R_{pAu} from p+Au collisions (blue star), and CMS results from Pb+Pb collisions at $\sqrt{s_{\mathrm{NN}}} = 2.76$ TeV (grey diamonds and magenta line) [7].

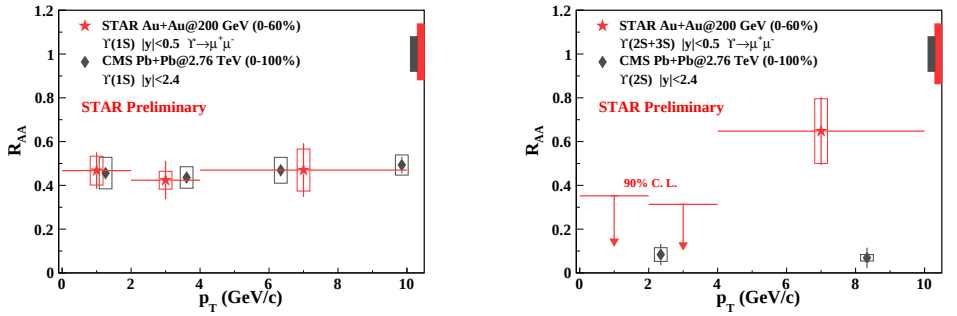

Figure 3: R_{AA} for the Υ(1S) (*left*) and the Υ(2S+3S) (*right*) at mid-rapidity as a function of p_{T} in Au+Au collisions at $\sqrt{s_{\mathrm{NN}}} = 200$ GeV (red stars) together with CMS results for Pb+Pb collisions at $\sqrt{s_{\mathrm{NN}}} = 2.76$ TeV (grey diamonds) [7].

Comparisons to theoretical predictions are shown in Fig. 4. These quarkonium production models in heavy-ion collisions differ mainly in the implementation of various CNM effects, recombination as well as their approaches to the quarkonium binding potential. The Strongly Binding Scenario (SBS) models use the internal energy as the heavy quark potential. It corresponds to a fast Υ dissociation and neglects random thermal energy transfers with the medium. Unlike SBS, the Weakly Binding Scenario (WBS) uses the free energy as the potential. The Strickland-Bazow model [8] studies the two scenarios with no CNM effects nor regeneration included. The model by Liu et al. [9] includes dissociation only for the excited states, and systematically under-predicts the suppression, hinting at further influence of CNM effects and/or direct Υ(1S) dissociation. Unlike the two previous models, the Emerick-Zhao-Rapp SBS model [4] takes into account CNM and regeneration effects. In summary, the data appear to favour the SBS-based model calculations.

4. Conclusions and outlook

We present recent measurements of Υ production at mid-rapidity with the STAR experiment. In p+p collisions of $\sqrt{s} = 200$ GeV, the new and more precise cross-section results are in solid agreement

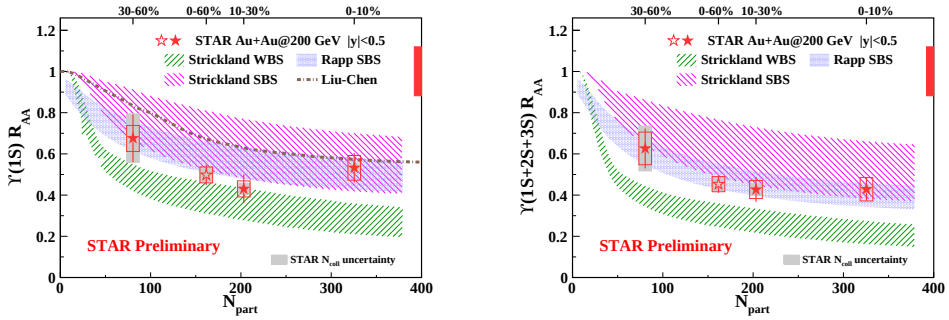

Figure 4: Nuclear modification factors for the Υ(1S) (*left*) and the Υ(1S+2S+3S) (*right*) in Au+Au collisions at $\sqrt{s_{\mathrm{NN}}} = 200$ GeV at mid-rapidity are shown as a function of the mean number of participants N_{part}. Also shown are the predictions of theoretical models [4][8][9].

with NLO CEM predictions as well as with the world-wide experimental data trend [6]. In p+Au collisions at $\sqrt{s_{\mathrm{NN}}} = 200$ GeV, the CNM effects are quantified via R_{pA}, which is measured to be $0.82 \pm 0.10(\mathrm{stat.})^{-0.07}_{+0.08}(\mathrm{syst.}) \pm 0.10(\mathrm{norm.})$.

In Au+Au collisions, we present R_{AA} as a function of N_{part} and p_{T} for the Υ(1S) and the Υ(2S+3S) separately. The Υ(1S) suppression at RHIC is similar to that at the LHC. Better understanding of CNM effects and the feed-down contribution is needed before drawing conclusions about direct Υ(1S) suppression. In the most central collisions, the Υ excited states are more suppressed than the ground state, which is in accordance with the sequential melting behaviour. The excited states also appear to be less suppressed at RHIC than at the LHC. These new Υ results can be further used to impose constraints on the QGP temperature at RHIC. Furthermore, analyses using other Au+Au data samples are under way, with a factor of two increase in statistics expected.

5. Acknowledgement

This work is supported by the grants CZ.02.1.01/0.0/0.0/16_013/0001569, LG15001, and LM2015054 (Brookhaven National Laboratory—participation of the Czech Republic) of Ministry of Education, Youth and Sports of the Czech Republic.

References

[1] T. Matsui and H. Satz, Phys. Lett. B **178**, 416 (1986).

[2] A. Mocsy, Eu. Phys. Jour. C **61**, 705 (2009).

[3] Z. Lin and C. Ko, Phys. Lett. B **503**, 104 (2001).

[4] A. Emerick, X. Zhao, R. Rapp, Eu. Phys. Jour. A **48**, 72 (2012).

[5] The STAR collaboration, Phys. Lett. B **735**, 127 (2014).

[6] A. Frawley, T. Ullrich, R. Vogt, Phs. Rev. **462**, 125 (2008).

[7] The CMS collaboration, Phys. Lett. B **770**, 357 (2017).

[8] M. Strickland and D. Bazow, Nucl. Phys. A **879**, 25 (2012).

[9] Y. Liu, B. Chen, N. Xu, P. Zhuang, Phys. Lett. B **697**, 32 (2011).

Measurements of the Upsilon Meson Production in Au+Au Collisions at $\sqrt{s_{\mathrm{NN}}} = 200$ GeV by the STAR Experiment

Oliver Matonoha, *for the STAR Collaboration*

Czech Technical University in Prague

Faculty of Nuclear Sciences and Physical Engineering

Venezia 2018 Quark Matter

Abstract

In ultra-relativistic heavy-ion collisions, creation of a novel state of matter, the quark-gluon plasma (QGP), has been observed. This hot, dense, and short-lived medium of deconfined quarks and gluons is experimentally very challenging to study. Suppressed production of heavy quarkonia, caused by colour screening of the binding force, has been viewed as a direct evidence of the QGP formation. Moreover, different quarkonium states are expected to dissociate at different temperatures, which can be used to constrain the properties of the medium. In this poster, we present recent measurements of the Υ production in Au+Au collisions at $\sqrt{s_{\mathrm{NN}}} = 200$ GeV via the di-lepton channel by the STAR experiment at RHIC. At RHIC energies, other phenomena influencing the quarkonium production, such as the regeneration and co-mover absorption, are expected to have little or no effect for the bottomonium family, which makes it a cleaner probe compared to the J/ψ meson.

Motivation

- **Quarkonium as a QGP thermometer**
  - A quarkonium is expected to dissociate by the colour screening effect in the hot medium if the Debye screening length becomes smaller than its radius:

    $r_{\mathrm{Debye}} < r_{\bar{Q}Q}$, $r_{\mathrm{Debye}} \propto T^{-1}$
  - This dissociation is dependent on the $\bar{Q}Q$ binding energy

    → ***Different $\bar{Q}Q$ states melt at different temperatures***

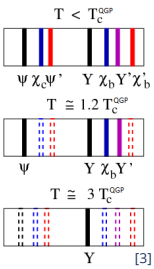

[3]

- **Upsilons at RHIC**
  - Due to the low $\bar{b}b$ cross-section, the Υs almost do not suffer from regeneration by statistical recombination [1]
  - Certain Cold Nuclear Matter (CNM) effects, such as the absorption by co-moving hadrons, are also deemed negligible [2]

    → ***Much cleaner probe of the screening effect than the J/ψ***

Experimental Setup

- **Solenoidal Tracker At RHIC (STAR)** is a detector designed for studying heavy-ion collisions, located in Brookhaven National Laboratory, USA. It has excellent particle identification (PID) capability and full azimuthal coverage. Most of the sub-detectors are immersed in a 0.5 T magnetic field.
- To measure the scarce Υs in the di-electron channel, we utilise mainly two STAR sub-detectors:

- **Time Projection Chamber (TPC)**

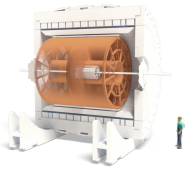

  - mid-rapidity coverage $|\eta| < 1.0$
  - tracking and momentum measurement
  - PID via ionisation energy loss dE/dx

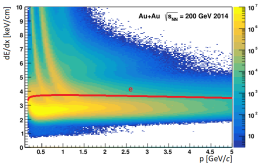

- **Barrel Electromagnetic Calorimeter (BEMC)**

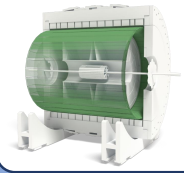

  - trigger on high-p_{T} electrons
  - electron identification via ratio of deposited energy to momentum

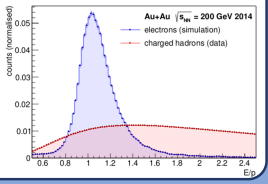

Dataset and Upsilon Reconstruction

- **Di-electron decay channel** is used to reconstruct the Υ ($\mathrm{BR}_{\Upsilon(1S)\to ee} = 2.38\%$)
- Data from Au+Au collisions at $\sqrt{s_{\mathrm{NN}}} = 200$ GeV taken in 2014
- A total of ~ 115M of **BEMC-triggered** events were analysed, corresponding to $\int L\,dt \sim 4\ \mathrm{nb}^{-1}$
- Υs were measured at $|y| < 0.5$, in 0-10%, 10-30%, and 30-60% centralities with primary tracks of $p > 3.5$ GeV/c; $|\eta| < 1.0$; $0.75 < E/p < 1.5$; $-1.5 < n\sigma^{dE/dx}_{\mathrm{electron}} < 3.0$

1. Online trigger on large energy deposition in BEMC towers (E_{T}>4.3 GeV)
2. One electron candidate reconstructed in the TPC is required to be matched to the triggering BEMC tower
3. The partner electron is also required to match with the BEMC
4. Apply further PID and quality cuts

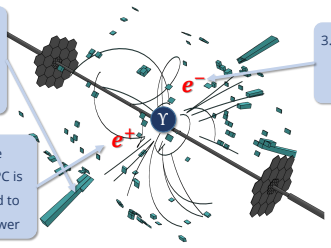

Raw Yield Extraction

- **Raw signal yield is extracted** using unbinned likelihood fit of the ***unlike-sign*** e^+e^- invariant mass spectrum
  - Combinatorial background estimated from the ***like-sign*** combinations
  - Fixed ***Υ(1S)*** and ***Υ(2S+3S)*** templates obtained from simulations incorporating full detector response
  - Shape of the correlated ***di-electron background***, mainly coming from $B\bar{B}$ decay and Drell-Yan, is determined from PYTHIA

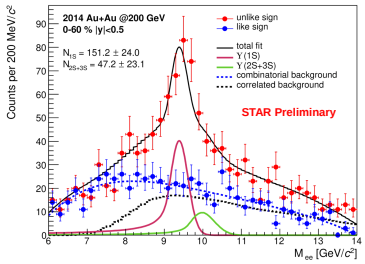

Acceptance and Reconstruction Efficiency

- ***Υ* signal from GEANT simulation of the detector response was embedded into real events** and used to determine the
  - Geometrical acceptance
  - Trigger efficiency
  - Tracking efficiency
  - BEMC PID efficiency
  - BEMC-TPC matching efficiency
- **High-purity electron sample** from photon conversions was used to obtain the
  - TPC PID efficiency

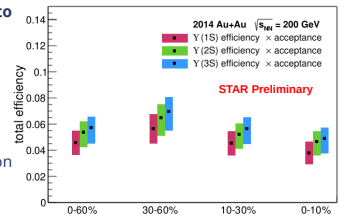

Results

- **Nuclear modification factor** is used to quantify the hot medium effect on the Upsilon production and is calculated as

$$R_{AA} = \frac{\sigma^{pp}_{inel}}{\langle N_{coll}\rangle} \frac{d^2N_{AA}/dp_T dy}{d^2\sigma_{pp}/dp_T dy}$$

- Results combined with other STAR measurements to increase the precision

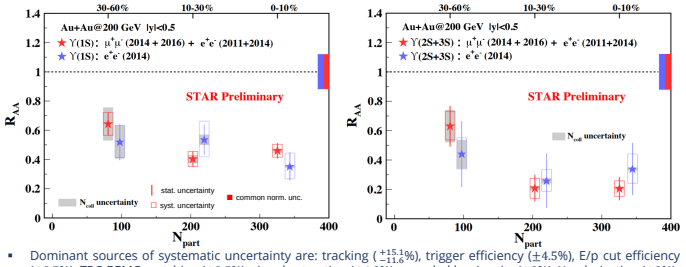

- Dominant sources of systematic uncertainty are: tracking ($^{+15.1}_{-11.6}$%), trigger efficiency (±4.5%), E/p cut efficiency (±8.7%), TPC-BEMC matching (±9.5%), signal extraction (±4.9%), sampled luminosity (±8%), Υ polarisation (±3%)

Conclusions

- Measurements of the Υ(1S) and Υ(2S+3S) in Au+Au collisions via the di-electron channel are presented using the 2014 data and combined with other STAR measurements
- Inclusive Υ(1S) is suppressed at RHIC with: $R_{AA}\,\big|^{0-10\%}_{|y|<0.5} = 0.46 \pm 0.05\ (stat.) \pm 0.04\ (syst.)$
- Υ(2S+3S) seem to be more suppresed than Υ(1S) in central collisions, consistent with the phenomenon of sequential melting, with: $R_{AA}\,\big|^{0-10\%}_{|y|<0.5} = 0.21 \pm 0.08\ (stat.) \pm 0.05\ (syst.)$

References

[1] A. Emerick, X. Zhao, R. Rapp, Eu. Phys. Jour. A **48**, 72 (2012).
[2] Z. Lin and C. Ko, Phys. Lett. B **503**, 104 (2001).
[3] H. Satz, Int. J. Mod. Phys. A **28**, 1330043 (2013).

Acknowledgement

This work was also supported by the grants LM2015054 and CZ.02.1.01/0.0/0.0/16_013/0001569 (Brookhaven National Laboratory - participation of the Czech Republic) of Ministry of Education, Youth and Sports of the Czech Republic.